# Implementation of state transfer Hamiltonians in spin chains with magnetic resonance techniques

Paola Cappellaro

## 1 Introduction

The goal of quantum state transfer (QST) is to map quantum information from one qubit to a distant one, for example in quantum communication protocols or in distributed quantum information processing (QIP) architectures. While photons are ideal carriers of quantum information, when state transfer is required in solid-state systems, between not too distant qubits, an alternative strategy [1] relies only on the natural evolution of a permanently coupled chain of quantum systems. Various systems have been proposed as experimental implementation of this scheme, including Josephson junction arrays [2], excitons and spins in quantum dots [3, 4], electrons in Penning traps [5] and ultracold atoms in a 1D optical lattice [6, 7]. Among all the proposed experimental systems, spins-1/2 stand out as the most natural one, thanks to the direct mapping from the theoretical model. Using electronic or nuclear spins as the physical basis for quantum wires can in addition take advantage of the well-developed techniques of magnetic resonance.

Spin systems are also at the center of many QIP proposals, starting from the famous scheme by Kane [8] and arriving to more recent proposals, including for example the Nitrogen Vacancy center in diamond [9]. In this context, it might be beneficial to use some of these spin qubits as quantum wires.

While no current implementation of magnetic resonance spin-based QIP has reached the level of control and complexity required for a scalable architecture, smaller-scale processors have been used to investigate quantum algorithms, including spin transport [10–13]. In general, magnetic resonance (and in particular nuclear magnetic resonance, NMR) plays an important role as a test-bed for a variety of questions related to QIP, from advanced control techniques to decoherence study, and it can make similar contributions in the study of quantum state transfer.

Paola Cappellaro

Nuclear Science and Engineering Department and Research Laboratory of Electronics, Massachusetts Institute of Technology, Cambridge, MA 01239 USA– e-mail: pcappell@mit.edu

More fundamentally, NMR has long been interested in the dynamics of transport, as transport of polarization and of correlated spin states can on one side elucidate the geometrical structure of molecules and crystals of interest [14], and on the other side it constitutes a crucial step in dynamical nuclear polarization (DNP) [15–17], which is used to achieve enhanced sensitivity. Thus, the investigation of quantum state transfer in NMR systems connects to and draws upon these prior studies and it can as well contribute to their advance.

This contribution is structured as follows. We first review in section (2) the basic principles of NMR, focusing on their applications to QIP problems. We present in particular liquid-state and solid-state NMR implementations of qubit systems, in sections (2.1) and (2.2), respectively. We then review in section (3) demonstrations of quantum state transfer in small liquid-state quantum information processors (Sec. 3.1) and in larger solid-state crystal systems (Sec. 3.2). We conclude the chapter with an outlook of the potential contribution of magnetic-resonance implementations both to the investigation of quantum state transfer beyond solvable models (exploring for example questions of decoherence) and to scalable QIP architectures.

## 2 NMR quantum information processing

Spin systems have been proposed as promising quantum information processing devices [8, 9, 18, 19] based on NMR techniques. Since the very start of experimental QIP, NMR has played an important role in implementing the first proof-of-principle demonstrations, thanks to the fact that it is mature technology [19–22]. Indeed, NMR is unique in that simple implementations based on liquid-state NMR have been able to control up to 12 spin qubits [23] with commercially available technology. There are three main reasons for the success of NMR QIP: well-defined qubits (and well characterized Hamiltonians), relatively long coherence times and a tradition of well developed (pulsed) control techniques.

**Spins –** In NMR-based QIP qubits are simply spin-1/2 nuclei, thus the mapping from logical to physical qubit is straightforward. The most common nuclear spins used in NMR are shown in table (1). Spins interact with magnetic fields via the

| Nucleus | Natural abundance | $\gamma$ (MHz/T) | $\omega_L$ at 9.4 T (MHz) | $\omega_L$ at 7.05 T (MHz) |
|---------|-------------------|------------------|---------------------------|----------------------------|
| $^1$H   | 99.99             | 42.58            | 400                       | 300                        |
| $^{13}$C | 1.1              | 10.71            | 100.7                     | 75.5                       |
| $^{15}$N | 0.366            | -4.316           | 40.6                      | 30.4                       |
| $^{19}$F | 100              | 40.05            | 376.5                     | 282.4                      |

**Table 1** Spin-$\frac{1}{2}$ nuclei commonly used in NMR QIP experiments. We report their isotopic natural abundance (%), their gyromagnetic ratios $\gamma$ and their Larmor frequencies $\omega_L = \gamma B$ at two typical NMR magnetic field strengths.
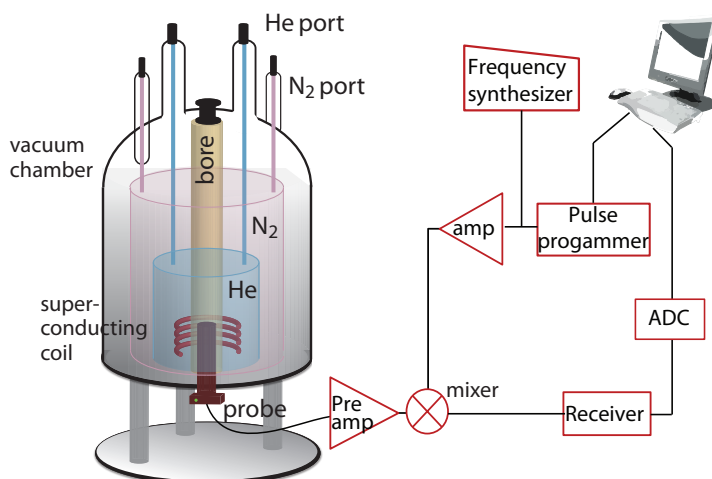
**Fig. 1** Schematic of the principal components of a NMR system. The sample is placed inside a probehead that carries a resonant circuit. The probehead is inserted in the bore of a superconducting magnet, kept at low temperature by liquid He (in turns kept cold by liquid Nitrogen). A radio-frequency (RF) field is amplified and gated by a computer-controlled timing unit and delivered via the resonant circuit to the sample. The time-dependent magnetic field produced by the sample is picked-up by the same coil, amplified, digitized and analysed by a computer. Components not shown here also allow for quadrature detection, phase, frequency and amplitude modulation of the RF field as well as the generation of gradient pulses.

Zeeman interaction [24–26], thus precessing at their Larmor frequency, set by the gyromagnetic ratio, $\omega_L = \gamma B$, which is proper of each isotope.

**Experimental apparatus –** The magnetic field is usually generated by a superconducting coil, which can create fields up to 23.5T with very good homogeneities. NMR QIP can take advantage of the mature technology, commercially available for NMR spectroscopy, as the basics operations are common for both tasks. The main components of the experimental apparatus are shown in figure (1).

**Measurement –** The spin magnetization is measured inductively by a pick-up coil. The measurement is weak, thus in contrast to projective measurements, the state is only weakly perturbed by the measurement and we can follow the evolution of the spin magnetization. The measurement is thus well-described by a simple model of a classical dipole, where the transverse spin magnetization couples to the coil via magnetic induction. Only the portion of the spin state that is dipolar and oriented along the coil axis will couple and be detected (although other parts of the density operator might evolve into detectable states during the measurement evolution time). The signal is the ensemble average of the transverse polarization over the whole sample.

**Pulse control –** The pick-up coil is used as well to manipulate the spins. The most common control technique in NMR is the use of short burst of magnetic field at the spin radio-frequency (RF) frequency $\omega_0$ in a transverse plane (with respect to the large, static magnetic field, by convention aligned with the z-axis). The Hamiltonian

describing the interaction of the spins with the RF field is given by:

$$\mathscr{H}_{ext} \;=\; e^{-i\varphi(t)\Sigma_z} \left( \tfrac{1}{2}\,\omega_{\mathrm{RF}}(t) \sum_h \sigma_x^h \right) e^{i\varphi(t)\Sigma_z} \tag{1}$$

where $\sigma_i$ are the usual Pauli matrices, $\Sigma_z = \sum_k \sigma_z^k$ and we set (here and in the following) $\hbar = 1$. Here $\varphi(t) = \omega_0 t + \phi(t)$ is a time-dependent phase and $\omega_{\mathrm{RF}}(t)$ is a time-dependent amplitude. The phase and amplitude can be controlled independently, allowing a high level of flexibility. Several methods such as shaped pulses [27], composite pulses [28] or numerically-optimized pulse shapes [29–31] have been used in NMR.

A host of pulse sequences have been developed in NMR to achieve various spectroscopic goals, as well as to improve the coherence properties of the system. These same techniques have had an influence on the further development of control strategies for QIP. We will now describe in more detail NMR experimental techniques applied to quantum information processing, making a distinction depending on the type of sample studied, either liquid- or solid-state.

## 2.1 Liquid-state NMR

Most of NMR spectroscopy deals with samples at the liquid state, investigating the spins in molecules. In liquid-state NMR the qubits are defined as magnetically distinct spins-$\frac{1}{2}$ of a given molecule, immersed in a solvent. Because of easy identification of qubits, good knowledge of their Hamiltonians and of the relaxation superoperator, high level of control already developed by the NMR community and long decoherence times, liquid-state NMR is recognized as one of the most flexible test-beds for QIP. One of its limitations is the exponential decrease in signal for each qubit added to the system, which is associated with the use of mixed states in ensemble QIP. Although not a scalable approach to quantum computation because of the limited number of frequency-resolved spins, liquid-state NMR has made it possible over the years to test experimentally quantum algorithms and to study issues of control and fault-tolerant quantum computation.

**Spin qubits –** In liquid-state NMR, the spin-carrying nuclei are part of molecules dissolved in a solvent. As the couplings among molecules are weak and averaged to zero to first order by random motion, the molecules can be considered independent. The NMR sample is then an ensemble of a large number ($N_m \approx 10^{18}$) independent molecules, or, in QIP terms, an ensemble of $N_m$ independent quantum processors.

**Hamiltonian –** The $N$ spins in each molecule are magnetically distinct: Not only different chemical species have different gyromagnetic ratios, but also the resonances of homonuclear spins depend on the local chemical environment. These differences in frequencies are called *chemical shifts* and are usually on the order of 10-100 part-per-million (ppm) of the resonance frequency.

The spins interact with each other indirectly, the coupling being mediated by the electrons forming the molecular orbital between nuclei. The interaction strength is

given by the *scalar (weak) coupling* constants $J_{k,h}$, which can range from a few Hz to hundreds of Hz.

The internal Hamiltonian of a molecule's nuclear spins in a large external magnetic field along the z-axis is then:

$$\mathcal{H}_{int} = \frac{1}{2}\sum_{k=1}^{N}\omega_k\sigma_z^k + \frac{\pi}{2}\sum_{k\neq h}J_{k,h}\sigma^k\cdot\sigma^h \tag{2}$$

where $\sigma_\alpha^k$ are Pauli matrices for the $k^{th}$ spin.

It is usual in NMR to work in the so-called *rotating* frame, an interaction frame defined by the RF driving frequency $\omega_0$ and the total spin in the $z$-direction, $\Sigma_z = \sum_k \sigma_z^k$. Thus the frequencies $\omega_k$ in Eq. (2) are to be interpreted as: $\omega_k = \omega_L^k + \delta\omega_k - \omega_0$, where $\omega_L^k$ is the Larmor frequency of the $k^{th}$ nucleus and $\delta\omega_k$ its chemical shift.

The values of the chemical shifts and J-couplings of a molecule's nuclear spins can be derived directly from their spectrum. For example, in Fig. (2) are the parameters of the internal Hamiltonian of one molecule used in QST experiments [13, 32].

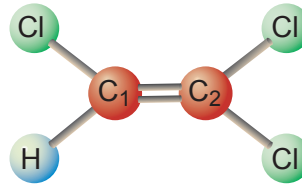|       | H     | $C_1$  | $C_2$  | $T_1$ | $T_2$ |
|-------|-------|--------|--------|-------|-------|
| H     | 3,233 |        |        | 4.7s  | 0.24s |
| $C_1$ | 201   | 14,660 |        | 3.8s  | 0.40s |
| $C_2$ | 9     | 103    | 15,566 | 4.2s  | 0.21s |



**Fig. 2** Carbon-13 labeled trichloroethylene. This molecule has been used for liquid-state NMR QIP experiments [13, 32]. The table on the left shows the NMR parameters. The diagonal terms in the table are the chemical shifts in Hz with respect to the reference frequencies 500.13 and 125.76 MHz, for $^1$H and $^{13}$C respectively. The non-diagonal terms are the $J$ coupling constants in Hz. Also reported are the measured [32] $T_1$ and $T_2$ times for each spin. The spins are labeled as in the figure on the right.

**Coherence Times** – Spin-1/2 systems have particularly long coherence times since they only couple to magnetic (and not electric) fields. In addition, they are shielded by the surrounding electronic spins. Thus the only source of decoherence is the coupling to other spins in the system. The longitudinal relaxation time $T_1$ –which describes energy exchange with the lattice and determines the relaxation to thermal equilibrium– can be extremely long, especially in solid-state systems, where it can reach minutes. The transverse relaxation time $T_2$ it is instead usually shorter in solid crystals, due to the dipolar couplings among spins. At the liquid-state, instead, because of the fast molecular reorientation, most of the spin couplings to other molecules are averaged, thus yielding $T_2$ coherence times of the order of hundreds of millisecond.

### 2.1.1 Liquid-state NMR quantum information processing

Liquid-state NMR has been one of the first techniques that has been able to demonstrate experimentally the concepts of quantum information processing. Thanks to the discovery of pseudo-pure states [33, 34] in 1997, many simple algorithms have been implemented in small NMR molecular systems. These include Deutsch's algorithm [35], which was implemented on homonuclear [36, 37] and heteronuclear [38] spin systems, as well as its generalization, the Deutsch-Josza algorithm [39], which was implemented on systems comprising from one to five spins [40] (the first implementation being on three spins [41]). Grover's quantum search algorithm [42] was implemented both in liquid-state NMR systems [43, 44] and in a liquid-crystal system [45]. The quantum Fourier transform was as well demonstrated in liquid-state NMR [46] as well as Shor's factorization algorithm [47]. Besides these algorithms, NMR was also used to study quantum simulations [48–50], quantum random walks [51], quantum games [52, 53] and quantum chaos [54]. Most of these results have been made possible by the creation of pseudo-pure states (see next section), which play as well a role in the demonstration of quantum state transport.

One of the most important contributions of NMR QIP has been in the precision with which qubits can be controlled. This includes advances in error-correction techniques, based on both active quantum error correction [55] and on passive protection via decoherence-free subsystems [56–61]; and development of robust control techniques (see section 2.1.3) to avoid coherent gate errors. These control techniques have also enabled the implementation of QST in small molecular systems and will be more generally useful in many future implementations of quantum state transfer.

### 2.1.2 Pseudo-pure states

The simulation of small quantum algorithms by ensemble liquid-state NMR has been made possible by techniques for the preparation of so-called pseudo-pure states that are able to simulate the dynamics of pure states:

$$\rho_{\text{pps}} = \frac{1-\alpha}{2^N} \mathbb{1} + \alpha |0\rangle\langle 0|^{\otimes N}, \tag{3}$$

where $N$ is the number of spins. Since the identity operator $\mathbb{1}$ is left unchanged by the usual unital evolution of NMR and does not contribute to the signal, the evolution of this pseudo-pure states is completely equivalent to the evolution of the associated pure states.

Pseudo-pure states can be obtained either by spatial [33] or temporal averaging [62] or by logical labeling [34]. In general, one needs to use a non-coherent evolution in order to obtain $\rho_{\text{pps}}$ from the thermal-equilibrium state,

$$\rho_{th} = \frac{e^{-\beta\mathscr{H}}}{Z} \approx \frac{\mathbb{1} - \varepsilon\Sigma_z}{2^N}, \tag{4}$$

where $\varepsilon = \beta \hbar \omega \ll 1$, with $\beta = (k_b T)^{-1}$ the Boltzmann factor and $\Sigma_z = \sum_{k=1}^{N} \sigma_z^k$. Since $\alpha < \varepsilon$, pseudo-pure states are still highly mixed states and they usually entail a signal loss.

For example, in temporal averaging one repeats the experiment several times with different preparation steps. The signal from each experiment measurement is averaged to give the final answer. Provided the preparation steps are chosen such that the average of the prepared input states is a pseudo-pure state, the signal average is the same as for a pure input state. This technique is somewhat reminiscent of phase cycling in NMR [63,64], in which the same sequence is repeated several times with different pulse phases, in order to select only a particular subsystem of the state (e.g. only the double-quantum terms [26]).

### 2.1.3 Control

NMR experiments have contributed greatly to the development of control strategies for QIP. Drawing on the expertise of NMR spectroscopy, the first algorithms were implemented by decomposing complex quantum gates into simpler units that could be implemented by a combination of RF pulses and evolution under the internal Hamiltonian. In addition, composite pulses [28], adiabatic pulses [65] and shaped pulses [66] were adopted in early NMR QIP experiments to better compensate for static and RF field inhomogeneities.

Since then, more sophisticated control techniques have been introduced. A particular promising direction has been in the development of numerical searches for the optimal excitation profile [67], either based on strongly modulated pulses [29] or by optimal pulse shapes [31]. The first method uses a numerical optimization to find strong control fields, which performs a desired spin selective unitary operation, without any additional corrections being required to account for decay or inhomogeneities. The second method, based on optimal control theory (OCT), finds analytical solutions to time-optimal realization of unitary operation, by optimization techniques based either on gradient methods [31] or on Krotov's numerical method [68].

NMR QIP has also contributed greatly to the development of dynamical decoupling techniques [69–71], which are aimed at improving the coherence times of quantum systems and build upon long-established NMR techniques such as spin echo [72] and CPMG sequence [73,74].

## 2.2 Solid-state NMR

Solid-state NMR presents some differences that are advantageous for QIP. With spins fixed in a solid matrix, the dipolar interactions are not averaged out. This provides much stronger couplings for faster gates, but also a shorter phase coherence time, which can be increased only by special purpose pulse sequences. In addition,

the spin polarization can be increased by dynamical nuclear polarization [16, 17], increasing the sensitivity.

The dominant interaction in spin-$\frac{1}{2}$ nuclear systems in a rigid crystal is the magnetic dipole-dipole interaction. The dipolar Hamiltonian is given by

$$\mathscr{H}_{dip} = \sum_{i<j} \frac{\hbar \gamma_i \gamma_j}{|r_{ij}|^3} \left( \frac{3(\boldsymbol{\sigma}_i \cdot \mathbf{r}_{ij})(\boldsymbol{\sigma}_j \cdot \mathbf{r}_{ij})}{|\mathbf{r}_{ij}|^2} - \boldsymbol{\sigma}_i \cdot \boldsymbol{\sigma}_j \right) \tag{5}$$

where $\mathbf{r}_{ij}$ is the intra-spin vector and $\gamma_i$ the gyromagnetic ratio of the i$^{th}$ spin.

In a large magnetic field along the z axis, we only consider the energy-conserving *secular* part of the dipolar Hamiltonian, that is, the terms that commute with the stronger Zeeman Hamiltonian (and therefore conserve the total magnetization along the z direction). The dipolar Hamiltonian then takes the form:

$$\mathscr{H}_{dip} = \sum_{ij} b_{ij} [\sigma_z^i \sigma_z^j - \frac{1}{2}(\sigma_x^i \sigma_x^j + \sigma_y^i \sigma_y^j)] \tag{6}$$

where the dipolar coupling coefficients are given by:

$$b_{i,j} = \frac{1}{2} \frac{\hbar \gamma_i \gamma_j \left[ 3\cos(\vartheta_{ij})^2 - 1 \right]}{|\mathbf{r}_{ij}|^3} \tag{7}$$

with $\vartheta_{ij}$ the angle between intra-spin vector and the external magnetic field direction, $\cos(\vartheta_{ij}) \propto \hat{\mathbf{z}} \cdot \mathbf{r}_{ij}$.

This many-body Hamiltonian drives a very complex dynamics; of particular relevance for quantum information transport are the dynamics of spin diffusion [17, 75–77] and of multiple quantum coherences [78–80]. The dynamics can be further tailored by multiple-pulse sequences. Various tools have been developed to describe the subsequent complex evolution and to guide in the design of pulse sequences, most notably average Hamiltonian theory (AHT) [81, 82]. This technique also plays an important role in engineering QST Hamiltonians.

### Average Hamiltonian theory and Hamiltonian engineering

The effects of a series of pulses and delays, organized in a cyclic sequence, can be best evaluated using Average Hamiltonian Theory (AHT) [81–83] which is an important tool in the construction of special purpose pulse sequences. The basic idea is that the evolution of the system under the applied periodic train of pulses may be described as if occurring under a time-independent effective Hamiltonian $\overline{\mathscr{H}}$. In a multiple pulse sequence, the cycle propagator over the duration $T_c$ of each control cycle reads

$$U(T_c) = \mathscr{T} \exp\left( -i \int_0^{T_c} [\mathscr{H}_{dip} + \mathscr{H}_{RF}(s)] ds \right) = e^{-i\overline{\mathscr{H}} T_c}, \tag{8}$$

where $\hbar = 1$, $\mathscr{T}$ denotes the time-ordering operator and $\mathscr{H}_{\mathrm{RF}}(t)$ is the time-dependent Hamiltonian describing the RF pulses. By invoking the Magnus expansion [82], the actual Hamiltonian $\overline{\mathscr{H}}$ may be expressed as $\overline{\mathscr{H}} = \sum_{\ell=0}^{\infty} \bar{\mathscr{H}}^{(\ell)}$, where the lowest-order term must yield the desired target Hamiltonian. We thus want to impose the condition:

$$\sum_k R_k \mathscr{H}_{dip} R_k^{\dagger} = \mathscr{H}_{des}, \tag{9}$$

where $R_k$ are collective rotations of all the spins given by the RF pulses. For cyclic and periodic pulse sequences, the long-time evolution over many cycles can be evaluated by simply calculating the evolution over one cycle, which in turn is well-approximated by the lowest-order AHT expansion. The higher order terms can be usually neglected, since $\left\| \bar{\mathscr{H}}^{(\ell)} \right\| = \mathscr{O}(T_c^{\ell})$.

In addition, if the pulse cycle is time-symmetric all odd-order corrections vanish [84], and the leading error term in the cycle propagator is of order $\mathscr{O}(\left\| \bar{\mathscr{H}}^{(2)} T_c \right\|)$. Remarkably, this is true even when considering ideal and finite-width pulses. Average Hamiltonian techniques are invaluable in achieving Hamiltonian engineering [85, 86] that can be used for a variety of QIP goals. Here we will use this technique to guide the engineering of the transport Hamiltonian [11].

## Multiple quantum coherences

Evolution under complex multiple-pulse sequences usually lead to the creation of many-body spin states. While creating these correlations is not in general the goal of quantum state transfer, one can gather further insight in the transport dynamics by characterizing these states experimentally. Since solid-state NMR does not allow single-spin readout, as required for example for state tomography, other techniques have been developed to characterize these many-spin states. In particular, it is critical to distinguish the presence of correlation among the spins, specially coherences.

In NMR, coherences between two or more spins are usually called *multiple quantum coherences* (MQC), to distinguish them from the single quantum coherence operators, which are the usual (direct) observables. Quantum coherence in general refers to a state where the phase differences among the various constituent of the system wavefunction can lead to interferences. In particular, quantum coherences often refer to a many-body system, whose parties have interacted and therefore show a correlation, a well defined phase relationship. When the system is quantized along the $z$ axis, so that the Zeeman magnetic moment along $z$ is a good quantum number, a quantum coherence of order $q$ is defined as the transition between two states $|m_1\rangle$ and $|m_2\rangle$, such that the difference of the magnetic moment along z of these states is $\propto m_1 - m_2 = q$. The matrix element in the system's density operator $|m_2\rangle\langle m_1|$ is also called a coherence of order $q$.

Quantum coherences can also be classified based on their response to a rotation around the z axis: A state of coherence order $q$ will acquire a phase proportional to $q$ under a z-rotation:

$$e^{-i\varphi \Sigma_z/2}\rho_q e^{i\varphi \Sigma_z/2} = e^{-iq\varphi}\rho_q \tag{10}$$

This property can be used to selectively detect a particular quantum coherence order.

Since higher quantum coherences are sensitive to the number, geometry and interconnectivity among nuclei, they can be used to access information about these properties, which are otherwise hidden in a simpler experiment. In particular, since a $q$-quantum coherence can only form in a cluster of $q$ or more spins, it is also possible to estimate the number of spins interacting at a given evolution time; this kind of experiments are called *spin-counting* experiments [80].

MQC intensities cannot be measured directly, since the NMR spectrometer coil is only sensitive to single body, single quantum coherences. MQC created in the system must therefore be tagged before bringing them back to observable operators, in order to separate the contributions of different MQC into the signal. The usual MQC experiment thus involves 4 steps (see Fig. 3).

During the preparation time, a pulse sequence creates a propagator $U_{MQ}$ that generates high coherence orders. The evolution period lets the system evolve to better characterize the MQC as required by each specific experiment. The refocusing step brings back the MQC to single-spin states, ideally by a propagator $U_{MQ}^{\dagger}$; finally, after a $\pi/2$ pulse, the signal is measured during the detection period. In the most simple experiment, the evolution period consists in the acquisition of a phase $\varphi$ (either by an off-resonance, free evolution period or more simply, by a phase shift of all the following pulses). The experiment than reveals the intensities of MQC created in the preparation time. Starting from the thermal state $\rho(0) \propto \mathbb{1} - \varepsilon\delta\rho_0$, where $\delta\rho_0 = \Sigma_z$, the observed signal is indeed given by:

$$\begin{aligned} S_{\varphi}(t) &= \text{Tr}\left\{U_{MQ}^{\dagger}e^{-i\varphi\Sigma_z/2}U_{MQ}\delta\rho_0 U_{MQ}^{\dagger}e^{i\varphi\Sigma_z/2}U_{MQ}\Sigma_z\right\} \\ &= \text{Tr}\left\{e^{-i\varphi\Sigma_z/2}\rho_{MQC}e^{i\varphi\Sigma_z/2}\rho_{MQC}\right\} = \sum_q e^{iq\varphi}\text{Tr}\left\{\rho_q\rho_{-q}\right\} \end{aligned} \tag{11}$$

where $\rho_q$ is the $q^{th}$-quantum coherence component in the state $\rho_{MQC} = U_{MQ}\Sigma_z U_{MQ}^{\dagger}$. In the last step we used Eq. (10) and the fact that $\text{Tr}\left\{\rho_p\rho_q\right\} = \delta_{p,-q}$ to simplify the expression. By varying the angle $\varphi$ between 0 and $2\pi$ in steps of $\pi/M$ ($M$ being the maximum coherence number to be measured), it is possible to obtain the intensities

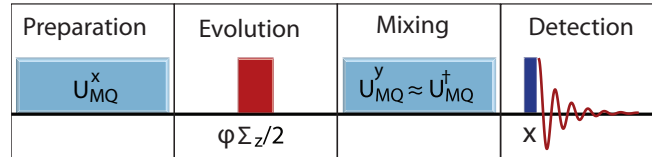| Preparation | Evolution | Mixing | Detection |
|---|---|---|---|
| $U_{MQ}^x$ | | $U_{MQ}^y \approx U_{MQ}^{\dagger}$ | |
| | $\varphi\Sigma_z/2$ | | x |

**Fig. 3** NMR pulse sequence for the creation and detection of MQC. The usual multiple quantum experiment is composed of four steps: The MQC are first excited during the preparation period (for example by a multiple quantum propagator $U_{MQ}^x$, see also Fig. 7). MQC evolve during the evolution period. In the simplest case a simple $\varphi$ rotation along the $z$ axis ($\varphi\Sigma_z/2$) is applied to flag each coherence in the system state. MQC are then refocused during the mixing periods (by $U_{MQ}^{\dagger}$) prior to measurement, obtained by a $\pi/2$ rotation followed by acquisition.

of the MQC contributions, by Fourier-transforming the signal with respect to $\varphi$:

$$I_q(t) = \sum_{m=1}^{2M} S_{\varphi_m}(t) e^{iqm\pi/M}, \tag{12}$$

where $S_{\varphi_m}(t) = \text{Tr}\{\rho_m(t)\rho_i\}$ is the signal acquired in the $m^{th}$ measurement for $\varphi_m = m\pi/M$.

## 2.3 Liquid crystals

To benefit from advantages of both liquid-state NMR (small number of spins with addressable frequencies) and solid-state NMR (strong dipolar couplings) molecules can be embedded in a liquid crystal matrix that fixes their orientations. Then, the dipolar couplings inside the molecules are not averaged out providing faster dynamics.

Liquid crystals are like liquids in that the constituent molecules undergo rapid translational diffusion, and they are like solids in that the molecules demonstrate some amount of long-range ordering. The NMR spectrum of a typical liquid crystal material is very broad due to the many non-equivalent dipolarly coupled protons. However, when a smaller, rigid molecule is dissolved in a liquid crystal solvent, the solute adopts the orientational ordering of the solvent and the resolved peaks of the solute spectrum appear on top of a broad baseline due to the liquid crystal solvent. Multiple pulse sequences can remove the unwanted signal from the solvent while leaving a complicated spectrum of many resolved transitions due to the dissolved molecules. The dominant features in the resolved spectrum arise due to the presence of strong magnetic dipolar couplings among nuclear spins in the solute material. This strong dipolar interaction is the principal difference between liquid and liquid crystal solvents NMR.

For an ensemble of rigid molecules, the inter-nuclear distances are fixed by the structure of the molecule, and the angular terms in the dipolar coupling strength are averaged over the distribution of molecular orientations in the ensemble $\langle b_{ij} \rangle = \frac{1}{2} \frac{\hbar \gamma_i \gamma_j \langle 3\cos(\theta_{ij})^2 - 1 \rangle}{|\mathbf{r}_{ij}|^3}$. In both liquid and liquid crystal solvents, the solute molecules move about with rapid, diffusive translational motion, which averages the intermolecular dipolar couplings to zero. In addition, the molecules in a liquid solvent are randomly rotating, averaging out the intramolecular dipolar couplings as well. By contrast, a molecule dissolved in a liquid crystal has a preferred orientation, so rotational motion is restricted, and intramolecular dipolar couplings are retained, as the average $\langle b_{ij} \rangle$ is non-zero.

The solute material in a liquid crystal solvent system can be used for NMR quantum information processing with the main advantage given by resolved, large dipolar couplings. This yields not only faster computing speed, but also the potential for

larger spin systems, thanks to the resolved couplings. Both of these advantages can be exploited in small-scale demonstrations of quantum state transfer [87].

# 3 Quantum state transfer in spin systems

The many contributions of NMR to quantum information processing have also extended to the area of quantum state transfer. There have been two main directions of exploration.

Liquid-state NMR systems have enabled proof-of-principle experiments demonstrating the concept of quantum state transfer (see section 3.1). While the system size is usually small, the long coherence time and high degree of control in these systems have allowed, for example, testing various QST strategies, such as faster transport with 3-body interaction and improved fidelity with end-chain control.

In solid-state NMR it is instead possible to explore larger spin systems and thus potentially longer chains. Exploiting the geometry of some crystals, which approximate one dimensional systems, it has been possible to achieve direct simulations of QST protocols (see section 3.2). In particular, this has increased the interest in quantum state transfer via mixed-state spin wires (Sec. 3.2.3). Current studies have focused on overcoming the constraints imposed by the collective control available in these systems to achieve the state preparation and readout required to observe quantum state transfer (Sec. 3.2.4). This has opened the possibility to gather further insight in the transport dynamics, taking into account effects that go beyond the solvable models (Sec. 3.2.5), an area where experimental implementations, such as those based on solid-state NMR, could give important contributions.

## *3.1 Simulations with liquid-state NMR*

As a testament to the versatility of liquid-state NMR experiments, the first observation of coherent transport by NMR was performed even before proposals for QST were put forward. Polarization transport (a "spin wave") was observed [10] in a 5 spin chain associated with Lysine. The dynamics was driven by the XX Hamiltonian,

$$\mathcal{H}_{xx} = \sum_{i,j} \frac{1}{2} b_{i,j} (\sigma_i^x \sigma_j^x + \sigma_i^y \sigma_j^y) = \sum_{i,j} b_{i,j} (\sigma_i^+ \sigma_j^- + \sigma_i^- \sigma_j^+) \tag{13}$$

obtained from the natural weak-coupling interaction via a multiple-pulse sequence. The initial perturbation state was created by transferring polarization from a proton spin to the first C-13 spin in the chain. The amount of polarization was monitored by measuring each spin (which are spectroscopically distinguished) and it showed the well-known behavior for polarization transport [11] for equal coupling chain ($J = 55$Hz).
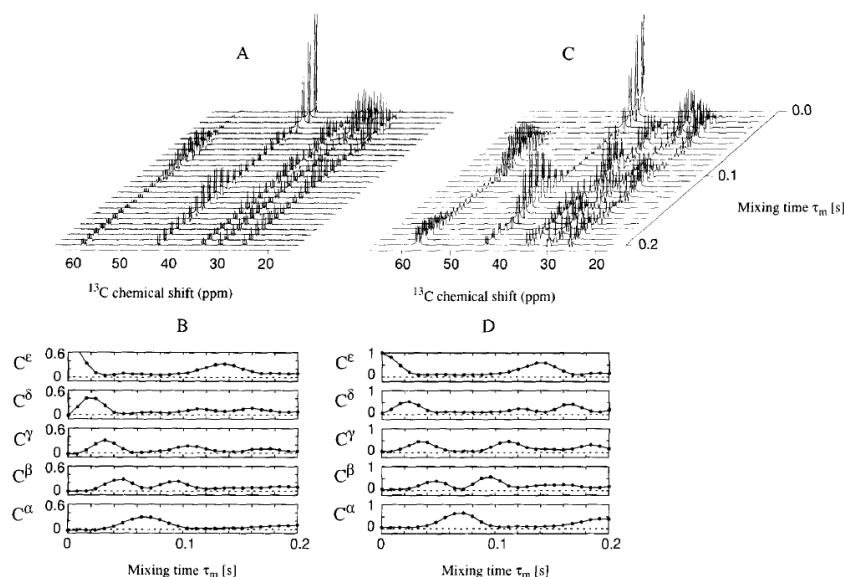
**Fig. 4** Experimental and simulation results reproduced with permission from Ref. [10]. A) shows experimental spectra (stacked plots) with soft pulse excitation on the first carbon in the chain ($C_\varepsilon$) recorded with increasing mixing time $\tau_m$ and (B) gives the corresponding peak integrals. (C) and (D) show the computer-simulated spectra and integrals using the experimental parameters (pulse widths, delays, chemical shifts and J couplings). The spectra were recorded at 100.6 MHz $^{13}$C Larmor frequency, selective excitation was achieved by a 2.5 ms Gaussian shaped pulse. Reprinted from Chemical Physics Letters, **268** (3), Z. Madi, B. Brutscher, T. Schulte-Herbruggen, R. Bruschweiler, R. Ernst, "Time-resolved observation of spin waves in a linear chain of nuclear spins", Pages 300-305 Copyright (1997), with permission from Elsevier.

For small spin chains, as found in small molecules observed by liquid-state NMR techniques, quantum state transfer can be obtained by manipulating individual spins to implement quantum gates, such as SWAP [88, 89] gates. In addition, CNOT gates [88] can be used to sequentially map the excitation of one spin at the end of the chain onto the other spins in the chain; this strategy, introduced in [90] to amplify the signal from a single spin, was implemented with NMR techniques [90–93].

However, the same transfer (and amplification) can be obtained relying on the evolution driven by spin-spin couplings; this alternative strategy can in principle lead to a transfer speed-up [94–96] thanks to optimal control techniques. More generally, QST driven by interactions between spins in the chain, without the requirement of single-spin control, is a more powerful paradigm that can in principle be implemented in larger spin chains. Thus, several authors have used liquid-state NMR, and the high degree of control that it provides, to simulate this scenario, even when individual control of spins was available – or indeed required to obtain the desired evolution.

J. Zhang and coworkers [13, 32] simulated QST driven by a simple XX Hamiltonian with equal coupling [97] in a 3-spin chain embodied by the spins in a

trichloroethylene (TCE) molecule (see Fig. 2). The experiments used a sample of $^{13}$C -labeled TCE dissolved in d-chloroform analysed in a Bruker DRX 500 MHz spectrometer. The proton spin $^1$H is taken as qubit 2, the $^{13}$C directly connecting to it is denoted as qubit 1, and the other $^{13}$C is qubit 3. The Hamiltonian of this system,

$$\mathscr{H}^{TCE} = \sum_{k=1}^{3} \omega_k \sigma_z^k + \frac{1}{2} \sum_{k,j>k} J_{kj} \sigma_z^k \sigma_z^j \qquad (14)$$

is quite different from the XX Hamiltonian $\mathscr{H}_{XX}$ on 3 spins required for transport. Thus the authors decompose the transport propagator, $U_{XX} = \exp(-it\mathscr{H}_{XX})$ into unitary propagators that can be implemented by liquid-state NMR techniques. Indeed, thanks to the difference in chemical shifts and $J$-coupling (Fig. 2), universal control can be achieved [98–100] and thus any propagator can be obtained. In the first implementation [32], the desired evolution was decomposed as:

$$U_{XX} = e^{-i\frac{\pi}{8}\sigma_x^1\sigma_z^2\sigma_y^3} e^{-i\frac{Jt}{\sqrt{2}}\sigma_x^1\sigma_x^2} e^{i\frac{\pi}{8}\sigma_x^1\sigma_z^2\sigma_y^3} e^{-i\frac{\pi}{8}\sigma_y^1\sigma_z^2\sigma_x^3} e^{-i\frac{Jt}{\sqrt{2}}\sigma_x^2\sigma_x^3} e^{i\frac{\pi}{8}\sigma_y^1\sigma_z^2\sigma_x^3} \qquad (15)$$

where each unitary is obtained by a combination of selective and non-selective RF pulses, interleaved by period of free evolution. It was realized that in this decomposition three-body interaction terms emerge naturally. These couplings are not present in the natural Hamiltonian, but can be introduced by the method proposed in [49]. The main limitation in the experimental results was due to the length of the pulse sequence, so that the fidelity of transport was limited by $T_2$-decay. Indeed the implementation via the decomposition in Eq. (15) was found to be longer and more complex than applying two SWAP gates, as needed for transport in a 3-spin chain.

The authors thus studied how to speed up the transport [13] exploiting these three-body Hamiltonian. They found that adding a term
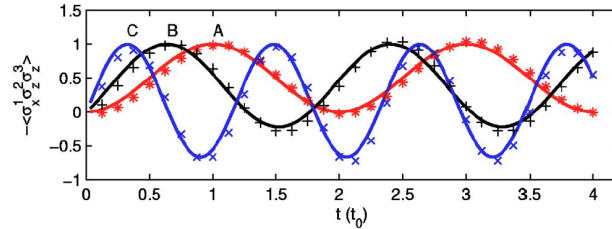


**Fig. 5** Implementation of QST in a molecule of TCE as obtained by Zhang *et al.* [13]. Overlap of the evolved density operator $\delta\rho(0) = \sigma_x^3$ with the target state $\sigma_x^1\sigma_z^2\sigma_z^3$, for different strengths of the three-body coupling as a function of time. Time is normalized to the transport time $t_0$ in the absence of the three-body interaction. Experimental data for $\lambda = 0$, 1.5 and 4 are marked by $\star$, $+$ and $\times$ respectively. The solid lines represent the theoretical results. Points A, B, and C indicate the maxima corresponding to the transfer times $C_3 \to C_1$. This clearly demonstrates the speed-up of the transfer by the three-body interaction. Reprinted figure with permission from J. Zhang, X. Peng, D. Suter, Phys. Rev. A **73**, 062325 (2006). Copyright (2006) by the American Physical Society.

$$\mathcal{H}_3 = \frac{\lambda}{2}(\sigma_x^1 \sigma_z^2 \sigma_x^3 - \sigma_y^1 \sigma_z^2 \sigma_y^3) \qquad (16)$$

to the Hamiltonian $\mathcal{H}_{XX}^{TCE}$ speeds up the transfer time for a wide range of the $\lambda$ parameter strength. This lead to a different decomposition of the transport propagator,

$$U_{XX}^{TCE} = U_C U_D = e^{-i2\sqrt{2}\mathbf{L}_C \cdot \mathbf{n}_C} e^{-i2\sqrt{2}\mathbf{L}_D \cdot \mathbf{n}_D} \qquad (17)$$

where $\mathbf{L}_C = [\sigma_x^1 \sigma_x^2/2, \sigma_y^2 \sigma_y^3/2, \sigma_x^1 \sigma_z^2 \sigma_x^3/2]$, $\mathbf{L}_D = [\sigma_x^2 \sigma_x^3/2, \sigma_y^1 \sigma_y^2/2, \sigma_y^1 \sigma_z^2 \sigma_x^3/2]$, $\mathbf{n}_C = \frac{1}{\sqrt{2}}[1, 1, \frac{4}{\lambda}]$ and $\mathbf{n}_D = \frac{1}{\sqrt{2}}[1, 1, -\frac{4}{\lambda}]$. The propagators where further decomposed in single-qubit operations and free evolution under the spin-spin coupling $e^{i\vartheta\sigma_z^i\sigma_z^k}$, which can be achieved by NMR techniques. Quantum state transfer was observed for initial mixed states, $\delta\rho_\alpha = \sigma_\alpha^3$ (with $\alpha = \{x, y, z\}$). These states were obtained using RF pulses and gradients to erase the polarization of spins 1-2. While in principle this is equivalent to following the state transfer evolution for a set of different initial states of the chain [13], no correction was taken to account for the phase arising in different excitation manifolds [101–104]. Despite the good agreement of the experimental data with the simulations shown in Fig. 5, the transport fidelity (measured by the correlation of the experimental state with the theoretical state) were quite low, $C \approx 0.2 - 0.3$. As in [32], the relatively low fidelity was due to relaxation processes, since the experimental implementation time ($t = 210 - 280$ ms) exceeds the dephasing time $T_2^*$. Further reductions arise from pulse errors and from the effects of strong couplings, which were ignored in the implementation. Thus, the speed-up offered by three-body terms is not enough in this case to avoid relaxation effects; in addition, it is hard to efficiently extend this strategy to longer chains, when a three-body Hamiltonian is not naturally present and single-spin addressability is not available.

Instead of relying on extensive single-spin control, Alvarez and coworkers [105] proposed to achieve perfect QST relying only on well-selected times of evolution under a (engineered) $\mathcal{H}_{XX}$ Hamiltonian and single-spin rotation about the $z$-axis, obtained by free evolution under the chemical shift. The alternation between these two evolution periods is able to select only the spin-spin couplings desired, thus the authors were able to implement QST along different pathways comprising different $^{13}$C spins in a leucine molecule backbone. Although the proposed method requires knowledge of system parameters and distinct frequencies for each spin in the chain as given by the chemical shifts, it is more general than the methods used in [13, 32], since it does not require selective qubit manipulations. This strategy is indeed closer to the Hamiltonian engineering strategy introduced in [85] for dipolarly coupled spin networks, where a combination of evolution under the double-quantum Hamiltonian and linear gradient is able to engineer an optimally-coupled [97] spin chain from a complex spin network.

Liquid-state NMR has also been used to simulate particular QST protocols, such as the strategy proposed in [106]. In this scheme, control gates are applied on the end-spins of the chain, which act as qubits; even in the presence of arbitrary couplings in the chain, the protocol achieves perfect transport fidelity by multiple it-

erations of spin chain evolution and two-qubit gate operations. The scheme was first implemented in a 3-spin chain in ethyl 2-fluoroacetoacetate [107] and later in a four-qubit chain based on orthochlorobromobenzene ($C_6H_4ClBr$) dissolved in the liquid-crystal solvent ZLI-1132 [87]. This last implementation exploited the larger spin couplings afforded by liquid-crystal NMR and adopted numerically optimized pulses (with the GRAPE algorithm [31]) to achieve higher fidelity of transport starting from an initial pseudo-pure state.

## 3.2 Spin chains in solid-tate NMR

Transport in complex many-body spin systems has been widely studied as it manifests itself as spin diffusion [76, 108, 109]. In a solid, diffusive behaviour driven by the naturally occurring secular dipolar Hamiltonian arises from energy-conserving flip-flops of anti-aligned spin pairs, which produce a dynamics analogous to a random walk. Spin diffusion has been studied extensively as it is a critical step of dynamic nuclear polarization [15–17], an important technique to increase the sensitivity of NMR. Unfortunately, the dipolar Hamiltonian-driven transport of magnetization in three dimensions appears indistinguishable from an incoherent process [110–112]. The polarization appears to decay to its thermodynamic equilibrium and thus spin diffusion cannot be used for QST. It was however realized early on that the dynamics can be different in one-dimensional, finite systems, where quasi-equilibrium regimes might emerge [113, 114]. This type of coherent behaviour was first observed in a ring of protons [115]. The six protons belonged to a benzene molecule; polarization was initially transferred to one of the proton spins by cross-polarization with a $^{13}C$ nucleus and eventually detected after mapping the evolved polarization intensity onto the $^{13}C$. As the benzene molecule was dissolved in a liquid crystal matrix of ZLI-1167, the spins interacted via the dipolar Hamiltonian which drove (imperfect) polarization transfer during a period of free evolution. The authors were thus able to contrast the polarization transfer in this small system – showing polarization oscillations– with the spin diffusion behaviour that leads to a polarization decay.

Still, the transport under the full dipolar Hamiltonian is slower than ballistic and dispersive and thus still not directly suitable for QST. However, solid-state NMR proved to be a good experimental test-bed for QST, since multiple pulse sequences can engineer the desired transport Hamiltonian. In the following we will describe a particular physical system, apatite crystals, that has been proven fruitful for the exploration of QST with solid-state NMR. We will then describe how a transport Hamiltonian can be engineered from the natural Hamiltonian and how transport can be studied even in the usual experimental NMR conditions, at room temperature with thermal equilibrium states. Control strategies for the manipulation of the equilibrium state allow the preparation of the initial state of interest for QST. Finally, we will describe how NMR techniques have allowed further exploration of the trans-

port dynamics and its limitations arising from control errors and interactions with the environment.

### 3.2.1 Apatite crystals for NMR-based QST

Owing to their unique geometry [116, 117], nuclear spin systems in apatite crystals have emerged as a rich test-bed to probe quasi-one-dimensional (1D) spin dynamics, including transport and decoherence [12, 118–120].

Apatite crystals have a hexagonal geometry with space group $P6_3/m$ [116, 121] (see Fig. 7). The main components of the apatite family are chlorapatite [ClAp, $Ca_{10}(PO_4)_6Cl_2$] and carbonated apatites: hydroxyapatite [HAp, $Ca_{10}(PO_4)_6(OH)_2$] and fluorapatite [FAp, $Ca_{10}(PO_4)_6F_2$]. The last two varieties have been studied extensively in NMR as they contain fluorine $^{19}F$ nuclear spins (FAp) or protons $^1H$ (HAp).

Crystals of FAp can be obtained easily as they occur naturally (e.g. well-known locations are in Durango, Mexico; Quebec, Canada; New Mexico or Connecticut, USA; Epirus, Greece) [122]. FAp and HAp can also be synthetically grown. For example, large single crystals of FAp have been grown by the Czochralski method [123, 124] and more recently by the flux method [125–127]. This same method has also been used to grow HAp [128]. Apatites have many diverse applications, from solid-state laser to fluorescent lamps, from phosphorus chemistry to geological probes. Calcium apatites have also applications in biology, since they form the mineral part of bone and teeth. FAp and HAp have thus become common as biocompatible materials for bone replacement and coating of bone prostheses and their growth methods have been optimized [128].

The parameters of the unit cell of FAp are $a = b = 9.367$ Å ; $c = 6.884$ Å; $\hat{a} = \hat{b} = 90°$ and $\hat{g} = 120°$ [129]. The $^{19}F$ nuclei form linear chains along the $c$-axis, each one surrounded by six other chains. The distance between two intra-chain $^{19}F$ nuclei is $d = c/2 = 3.442$ Å and the distance between two cross-chain $^{19}F$ nuclei is $D = a = 9.367$ Å. Due to the $1/r^3$ dependence of dipolar coupling, there is a large difference between the in-chain and cross chain couplings The largest ratio between the strongest intra- and cross-chain couplings is obtained when the crystalline $c$-axis is oriented parallel to the external field,

$$\frac{|3\cos(\vartheta_{in})^2 - 1|/r_{in}^3}{|3\cos(\vartheta_\times)^2 - 1|/r_\times^3} = \frac{2/d^3}{1/D^3} \approx 40$$

Thus, to first approximation, in this crystal orientation the 3D $^{19}F$ system may be treated as a collection of identical 1D spin chains. For a single chain oriented along $z$, we have $b_{j\ell} = -(\mu_0/\pi)(\gamma^2\hbar/c^3|j - \ell|^3)$. HAp crystals have a similar geometry, with parameters $D = 9.42$Å and $d = 3.44$Å [130].

Naturally occurring defects in the sample (such as vacancies or substitutions [122, 131–133]) cause the chains to be broken into many shorter chains. Natural crystals usually contain more impurities (as manifested by a shorter $T_1$ time and a yellow

color) and are thus expected to have shorter chain lengths. Synthetically grown crystals present quite long $T_1$ times (e.g. $T_1=1100$ s for $^{19}F$ [134]) indicating a low concentration of paramagnetic impurities; although other defects interrupting the chains, such as vacancies, are expected to be present, the chain length is likely longer.

**Fig. 6** Unit cell of fluorapatite crystal [$Ca_5(PO_4)_3F$], highlighting the geometry of the fluorine chains (red spheres). Blue spheres are calcium atoms, green are oxygen atoms and yellow, phosphorus atoms.
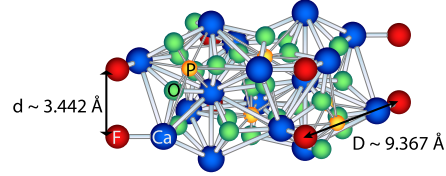


The dynamics of these spin chains have been studied by various nuclear magnetic resonance (NMR) techniques [120, 121, 130, 135–141].

This system first attracted the attention of experimentalists and theoreticians interested in characterizing the NMR spectrum of solid-state systems. While this is a formidable task for 3D systems, this quasi-1D system allowed the comparison of various approximation models, in particular the moment approximation, with numerical calculations and experiments [121, 135, 136]. Magic-angle spinning NMR was later used to characterize this crystal system, in particular various defects and dopant sites of technological interest [137, 141]. Multiple quantum coherence techniques were later used to further characterize the system [138]; conversely, the system was used to gain a better insight into the dynamics of MQC [120, 130, 139] and discrepancies with theoretical models adopted for MQC growth in 3D systems lead to further theoretical analysis [142, 143]. More recently, FAp crystals have been proposed as a quantum information processing platform [18, 144] and used to study quantum information transport [12, 101, 118, 119, 134] in a quasi-1D nuclear spin system, as we will present in the following.

### 3.2.2 Double-quantum Hamiltonian for spin transport

Most of the theoretical proposals for QST focused on the XX Hamiltonian, $\mathcal{H}_{XX}$ (Eq. 13), as the interaction driving the transport [145], whereas some studied the Heisenberg isotropic Hamiltonian [1] or the Ising Hamiltonian with a transverse field [104]. Unfortunately none of these Hamiltonian can be obtained from the naturally occurring dipolar Hamiltonian $\mathcal{H}_{dip}$ using only collective rotations, which are experimentally available. Indeed, following Average Hamiltonian Theory, we can obtain a desired Hamiltonian from the naturally occurring $\mathcal{H}_{dip}$ by piece-wise constant evolution under rotated versions of $\mathcal{H}_{dip}$, $\sum_k R_k \mathcal{H}_{dip} R_k^\dagger = \mathcal{H}_{des}$ (see Eq. 9). To highlight its rotation properties, we can write a general Hamiltonian for 2 spin-$\frac{1}{2}$ particles in terms of spherical tensors $T_{l,m}$ [146] (see Table 2):

$$\mathscr{H} = \sum_{l,m} (-1)^m A_{l,m} T_{l,m} \tag{18}$$

where the coefficients $A_{l,m}$ depend on the type of spin-spin interaction and the external field. Since collective rotations conserve the rank $l$ of each spherical tensor [82], there are limitations to which Hamiltonians can be engineered. In particular, $T_{00}$ (the isotropic Hamiltonian) commutes with collective rotations: its contribution is thus a constant of the motion and, conversely, it cannot be introduced in the desired Hamiltonian if it is not present in the natural one. An Ising Hamiltonian $\mathscr{H}_I = \sigma_z \sigma_z$ is instead expanded as $\mathscr{H}_I = (T_{00} + \sqrt{2}T_{20})/\sqrt{3}$, so that only the second part can be modulated. Conversely, the secular dipolar Hamiltonian is given by $T_{20}\sqrt{6}$, thus it cannot produce a Hamiltonian containing $T_{00}$, for instance we cannot generate the XX Hamiltonian $\mathscr{H}_{XX} = (T_{00} - T_{20}/\sqrt{2})/\sqrt{3}$. We can instead generate the Hamiltonian

$$\mathscr{H}_{DQ} = \sum_{i,j} \frac{1}{2} b_{i,j}(\sigma_i^x \sigma_j^x - \sigma_i^y \sigma_j^y) = \sum_{i,j} b_{i,j}(\sigma_i^+ \sigma_j^+ + \sigma_i^- \sigma_j^-) \tag{19}$$

which is usually called double quantum (DQ) Hamiltonian, since it can increase the coherences number by steps of two. As we will see, this Hamiltonian can be used to simulate QST. The DQ Hamiltonian can be prepared from the secular dipolar Hamiltonian by using a simple sequence consisting of two time intervals, $t_1 = t_2/2$ with the Hamiltonian rotated by a $\pi/2$ rotation around the y axis ($\frac{\pi}{2}\big|_y$) in second time period, to yield: $\sqrt{6}T_{2,0}t_1 + \left[\frac{3}{8}(T_{2,2} + T_{2,-2}) - \sqrt{\frac{1}{2}}T_{2,0}\right]t_2 \propto \mathscr{H}_{DQ}$. Symmetrized versions of this simple sequence are routinely used in NMR experiments [78,147]. The primitive pulse cycle is given by P2 $= \frac{\delta}{2} - \frac{\pi}{2}\big|_x - \delta' - \frac{\pi}{2}\big|_x - \frac{\delta}{2}$, where $\delta' = 2\delta + w$, $\delta$ is the delay between pulses and $w$ is the width the $\pi/2$ pulse (see Fig. 7). To first order average Hamiltonian, this sequence simulates the DQ Hamiltonian, while the 8-pulse sequence, P8 $=$ P2$\cdot\overline{\text{P2}}\cdot\overline{\text{P2}}\cdot$P2, where $\overline{\text{P2}}$ is the time-reversed version of P2, gives $\overline{\mathscr{H}}_{\text{DQ}}$ to second order and the 16-pulse sequences, P8$\cdot\overline{\text{P8}}$, compensates for pulse errors.

While the XX and DQ Hamiltonian are quite different (the first one conserves the total $\Sigma_z$ quantum number, whereas the second one can create high coherence terms) they differ by just a similarity transformation, $V_{XX}^{DQ}$. This transformation is

| | |
|---|---|
| $\mathbb{1}$ | $T_{00} = (\sigma_x^a \sigma_x^b + \sigma_y^a \sigma_y^b + \sigma_z^a \sigma_z^b)/\sqrt{3}$ |
| $T_{10}^a = \sigma_z^a/2$ | $T_{10}^b = \sigma_Z^b/2$ |
| $T_{11}^a = \sigma_+^a/\sqrt{2}$ | $T_{1-1}^a = \sigma_-^a/\sqrt{2}$ |
| $T_{11}^b = \sigma_+^b/\sqrt{2}$ | $T_{1-1}^b = \sigma_-^b/\sqrt{2}$ |
| $T_{11} = (\sigma_+^a \sigma_z^b - \sigma_z^a \sigma_+^b)/2$ | $T_{1-1} = (\sigma_-^a \sigma_z^b - \sigma_z^a \sigma_-^b)/2$ |
| $T_{10} = (\sigma_+^a \sigma_-^b - \sigma_-^a \sigma_+^b)/2$ | $T_{20} = (2\sigma_z \sigma_z - \sigma_x^a \sigma_x^b - \sigma_y^a \sigma_y^b)/\sqrt{6}$ |
| $T_{21} = (\sigma_+^a \sigma_z^b + \sigma_z^a \sigma_+^b)/2$ | $T_{2-1} = (\sigma_-^a \sigma_z^b + \sigma_z^a \sigma_-^b)/2$ |
| $T_{22} = \sigma_+^a \sigma_+^b/2$ | $T_{2-2} = \sigma_-^a \sigma_-^b/2$ |

**Table 2** Spherical tensors for two spin-1/2 (*a* and *b*) [146]. $\sigma_\alpha$ are the usual Pauli operators.
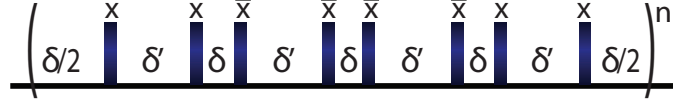
**Fig. 7** NMR pulse sequence for the creation of the DQ Hamiltonian. Here we show a 8-pulse sequence used in the experiments to create the DQ Hamiltonian, generating the propagator $U_{MQ}^x$. Bars are $\pi/2$-pulses along the $x$ or $\bar{x} = -x$ axis. The time delays between pulses are $\delta$ and $\delta' = 2\delta + w$, where $w$ is the duration of the $\pi/2$ pulses. Shifting the pulse phases by $\pi/2$ (that is, pulsing along $y$) we obtain the propagator $U_{MQ}^y = (U_{MQ}^x)^\dagger$.

particularly simple in one dimension, where a $\pi$ rotation of every other spin around the $y$ axis transforms $\mathcal{H}_{XX}$ into $\mathcal{H}_{DQ}$. This fact was used in [11, 148] to deduce the dynamics induced by $\mathcal{H}_{DQ}$ based on the well-known eigenvalue structure of $\mathcal{H}_{XX}$ [149]. In addition, it was realized [11] that for chains at thermal equilibrium, the initial state and the desired observable (magnetization of the end-chain spins) are left unchanged by the transformation $V_{XX}^{DQ}$ linking the XX and DQ Hamiltonian. This opened the possibility to study QST via solid-state NMR techniques.

### 3.2.3 Transport with mixed-state spin chains

With some notable exceptions (e.g., [104, 150–152]) where protocols for perfect state transfer without state initialization have been investigated under the assumption of sufficient end-chain control, existing analyses have primarily focused on transport in the one-spin excitation manifold. However, the assumption of reduced control on the spin chain, which is commonly used, may also naturally entail an imperfect initialization of the spin chain, possibly in a mixed state. Allowing QST via a mixed-state chain can considerably relax the experimental requirements and indeed it allowed its implementation via solid-state NMR.

We can generalize the spin excitation transport usually considered in QST to mixed-state chains by studying polarization transport. Thus, instead of an initial state $|00\ldots 1_j\ldots 0\rangle$, we take the state

$$\rho = \frac{1}{2^n}(\mathbb{1} + \varepsilon\,\delta\rho_z^j), \quad \delta\rho_z^j = \mathbb{1}_{j-1} \otimes \sigma_z^j \otimes \mathbb{1}_{n-j}. \tag{20}$$

This state represents a completely mixed-state chain with a single spin partially polarized along the z axis. To quantify the transport efficiency from spin $j$ to spin $l$, instead of the transport fidelity we evaluate the correlation between the resulting time-evolved state and the intended final state, that is, $M_{jl}(t) = \mathrm{Tr}\{\rho_j(t)\rho_l\}$. As long as the dynamics is unital, this is equivalent to $C_{jl}(t) = \mathrm{Tr}\{\delta\rho_z^j(t)\delta\rho_z^l\}/\mathrm{Tr}\{\delta\rho_z^j(0)^2\}$, since we only need to follow the evolution of the traceless deviation $\delta\rho$ from the identity. Since the state in Eq. (20) does not reside

in the lowest excitation manifold, in which QST is usually calculated, we need to evaluate the dynamics of the transport Hamiltonian in all the manifolds.

We consider first the XX-Hamiltonian [Eq. (13)]: as it conserves the spin excitation number, it can be diagonalized in each excitation subspace. We denote the eigenstates in the first excitation subspace by $|E_k\rangle$. Then, eigenfunctions of the higher manifolds can be exactly expressed in terms of Slater determinants of the one-excitation manifold. For example, given a basis for the 2-excitation manifold, $|pq\rangle = |0...1_p..0..1_q...0\rangle$, the eigenstates $|E_{kh}\rangle$ are

$$|E_{kh}\rangle = \frac{1}{2} \sum_{pq} \left( \langle E_k|p\rangle\langle E_h|q\rangle - \langle E_k|q\rangle\langle E_h|p\rangle \right) |pq\rangle, \tag{21}$$

with eigenvalues $E_{kh} = \hbar(\omega_k + \omega_h)$. We can then calculate the time evolution as [101]

$$U_{xx}(t)|pq\rangle = \sum_{k,h} e^{-i(\omega_k+\omega_h)t} \langle E_{kh}|pq\rangle\langle rs|E_{kh}\rangle |rs\rangle = \sum_{r,s} A_{pq,rs}(t)|rs\rangle, \tag{22}$$

where

$$A_{pq,rs}(t) = \begin{vmatrix} A_{pr}(t) & A_{ps}(t) \\ A_{qr}(t) & A_{qs}(t) \end{vmatrix}, \tag{23}$$

and $A_{pr}(t)$ describes the amplitude of the transfer in the one-excitation manifold, $A_{pr}(t) = \langle r|U_{xx}(t)|p\rangle$. Notice that the transport fidelity from spin $i$ to spin $j$ is then $F_{ij} = |A_{1N}|^2$.

More generally, for an arbitrary initial eigenstate of $\Sigma_z$, $|\mathbf{p}\rangle = |p_1, p_2, \ldots\rangle$, with $p_k \in \{0, 1\}$, the transfer amplitude to the eigenstate $|\mathbf{r}\rangle$ is given by

$$A_{\mathbf{pr}}(t) = \begin{vmatrix} A_{p_1 r_1}(t) & A_{p_1 r_2}(t) & \ldots \\ A_{p_2 r_1}(t) & A_{p_2 r_2}(t) & \ldots \\ \ldots & \ldots & \ldots \end{vmatrix}. \tag{24}$$

We can then evaluate the transfer of any initial mixed state $\rho_a = \sum_{\mathbf{p},\mathbf{q}} a_{\mathbf{pq}} |\mathbf{p}\rangle \langle \mathbf{q}|$ to another mixed state $\rho_b$ by calculating the relevant correlation between the evolved state and the final desired state,

$$M_{ab}(t) = \sum_{\mathbf{r},\mathbf{s},\mathbf{p},\mathbf{q}} b_{\mathbf{rs}} a_{\mathbf{pq}} A_{\mathbf{pr}}(t) A_{\mathbf{qs}}^*(t). \tag{25}$$

To implement QST in solid-state NMR with mixed-state chains, we are interested in the transport features of DQ-Hamiltonian. As this Hamiltonian does not conserve the spin excitation number, $[\mathscr{H}_{DQ}, \Sigma_z] \neq 0$, we would not expect it to support the transport of single-spin excitations. However, the DQ-Hamiltonian commutes with the operator $\tilde{\Sigma}_z = \sum_j (-1)^{j+1} \sigma_z^j$ and it can be block-diagonalized following the subspace structure defined by the (degenerate) eigenvalues of $\tilde{\Sigma}_z$. Different non-spin-excitation conserving Hamiltonians have been proposed in [104, 153, 154] taking advantage of other conserved quantities. The DQ-Hamiltonian allows for the mirror

inversion of states contained in each of the subspaces defined by the eigenvalues of $\tilde{\Sigma}_z$ (the equivalent of single-spin excitation and higher excitation manifolds for $\Sigma_z$). For pure states, these states do not have a simple interpretation as local spin excitation states, and the DQ-Hamiltonian is thus of limited practical usefulness for state transfer. Interestingly, however, the situation is more favorable for the transport of spin polarization in mixed-state chains. Indeed, states such as $\delta\rho_z^j$ are invariant, up to a sign change, under the similarity transformation from $\mathcal{H}_{xx}$ to $\mathcal{H}_{DQ}$. Thus we can recover the results obtained for the polarization transport under the XX-Hamiltonian for any coupling distribution:

$$C_{jl}^{DQ}(t) = (-1)^{j-l}|A_{jl}(t)|^2. \tag{26}$$

In figure (8) we illustrate the transport of polarization from spin $j = 1$ as a function of the spin number $\ell$ and time. Comparing transport under the equal-coupling XX- and DQ-Hamiltonians, we see enhanced modulations due to the positive-negative alternation of the transport on the even-odd spin sites. Despite this feature, transport properties of the two Hamiltonians are equivalent.
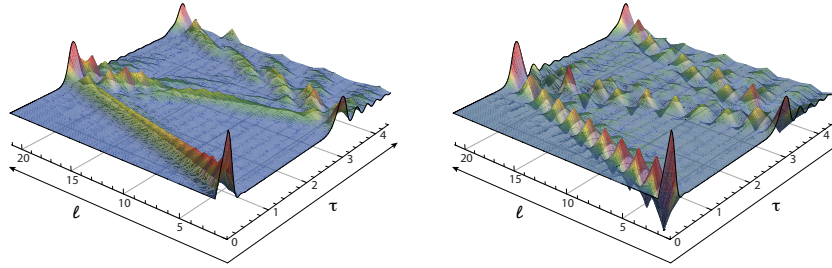


**Fig. 8** (Left) Transport of polarization under the XX-Hamiltonian. We assumed all equal couplings $b_{j,j+1} = b$. Shown is the intensity of the polarization at each spin site $C_{1,\ell}^{xx}(t) = P_{1,\ell}^{xx}(t)$ as a function of normalized time $\tau = bt$ for a propagation starting from spin 1. The chain length was $n = 21$ spins. (Right) Transport of polarization under the DQ-Hamiltonian $C_{1,\ell}^{DQ}(t)$ with the same parameters as in (Left).

While polarization transfer follows the same dynamics as the transport of a single-spin excitation, a similar mapping cannot be carried further in such a simple way. Thus we can transfer one bit of classical information, by encoding it in the sign of polarization, but we cannot use for example the state $\delta\rho_x^j = \mathbb{1}_{j-1} \otimes \sigma_x^j \otimes \mathbb{1}_{n-j}$ to simulate the transfer of a coherent pure state such as $|+\rangle|00...\rangle$, where $|+\rangle = (|0\rangle + |1\rangle)/\sqrt{2}$. The problem is that the evolution of this state creates a highly correlated state, as $\sigma_x^1$ evolves to $\prod_{i=1}^{n-1}\sigma_z^i\sigma_\alpha$, where $\alpha = x(y)$ for $n$ odd (even) [155]. Although particle-conserving Hamiltonians (such as the ones considered) allow for state transfer in any excitation manifold (and mirror-symmetric Hamiltonians achieve perfect state transfer), a manifold-dependent phase is associated with the

evolution [102, 156–158], thus only states residing entirely in one of these manifolds can be transferred.

To overcome this problem in mixed-state chain QST, two strategies have been proposed. Although the evolved state contains complex many-body correlations, quantum information can still be extracted from it with just a measurement [104], at the cost of destroying the initial state and of introducing classical communication and conditional operations. The second strategy is a simple two-qubit encoding [101, 151]. For evolution under the XX-Hamiltonian, the encoding corresponds to the zero-eigenvalue subspace of the operator $\sigma_z^1 + \sigma_z^2$, which corresponds to an encoded pure-state basis $|0\rangle_L^{xx} = |01\rangle$ and $|1\rangle_L^{xx} = |10\rangle$. Instead, for transport via the DQ-Hamiltonian, the required encoding is given by the basis $|0\rangle_L^{DQ} = |00\rangle$ and $|1\rangle_L^{DQ} = |11\rangle$, as follows from the similarity transformation between XX- and DQ-Hamiltonians. With this encoding we can transport a full operator basis,

$$
\sigma_L^{DQ} = \frac{\sigma_x^1 \sigma_x^2 - \sigma_y^1 \sigma_y^2}{2} \qquad \sigma_{yL}^{DQ} = \frac{\sigma_y^1 \sigma_x^2 + \sigma_x^1 \sigma_y^2}{2}
$$
$$
\sigma_{zL}^{DQ} = \frac{\sigma_z^1 + \sigma_z^2}{2} \qquad \math1_L^{DQ} = \frac{\math1 + \sigma_z^1 \sigma_z^2}{2}. \tag{27}
$$

thus we can transport one qubit of quantum information. This encoding protocol is quite versatile. For example, it can be extended to more than a single logical qubit, to encode an entangled state of two logical qubits into four spins [60, 159], such as an encoded Bell state $|\psi\rangle = (|01\rangle_L + |10\rangle_L)/\sqrt{2}$. With a small encoding overhead, in principle this allows perfect transport of entanglement through a completely mixed chain (see figure 9).
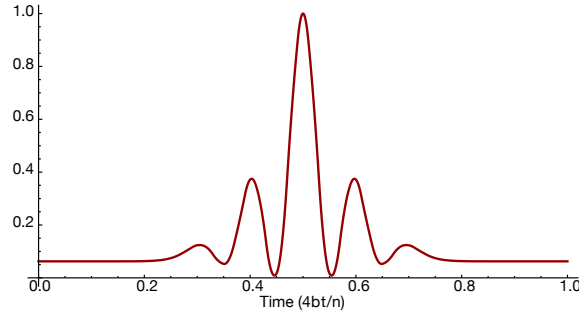


**Fig. 9** Transport fidelity of the logical entangled state $(|00\rangle_L + |11\rangle_L)/\sqrt{2} = (|0000\rangle + |1111\rangle)/2$ in a completely mixed chain of $n = 11$ spins. Here we assumed that the spins in the chain were coupled in a optimal way, with $b_{j,j+1} = b\sqrt{j(n-j)}/n$ [97, 101] and we plotted the fidelity as a function of the normalized time $bt/n$.

### 3.2.4 Chain initialization and readout

As explained in the previous section, transport of quantum information is possible even via a completely mixed-state spin chain. Still, one spin at the end of the chain should act as a qubit and initially encode the quantum information to be transferred. In a distributed architecture, the qubit might be a different physical system that is put in contact with the spin wire when transport is required. In NMR-based experimental efforts to demonstrate QST, the qubit is often the spin at the end of the chain [12, 134]. Thus we would like to initialize it in a state of interest for the transfer of either classical or quantum information, while leaving the rest of the spin chain in the maximally mixed state. In the first case, we would like to prepare the state $\delta\rho_z^1$ (see Eq. 20); whereas in the second case we would like to prepare one of the logical states, e.g., $\delta\rho_y^L = \frac{\sigma_y^1\sigma_x^2 + \sigma_x^1\sigma_y^2}{2} \otimes \mathbb{1}_{n-2}$ (see Eq. 27). Unfortunately, collective control of all the pulses in the chains, as given by on-resonance RF pulses, seems to preclude the preparation of these states. However exploiting the spin natural dynamics and a combination of coherent and incoherent control it is possible not only to prepare [12], but even to detect these types of states [134]. This was one critical step toward the demonstration of QST in a solid-state NMR platform.

The key insight was to realize that even in the absence of frequency addressability, the dynamics of the end-chain spins under the internal dipolar Hamiltonian is different from the bulk spins, as the end-spins have only one nearest neighbour.

Polarization initially in the transverse plane, $\delta\rho = \sum_{k=1}^{N} \sigma_x^k$ (prepared from the thermal state by a $\pi/2$ pulse), evolves under the internal dipolar Hamiltonian at different rates. The end-spin evolution rate is slower by a factor $\approx 1/\sqrt{2}$ as compared to the rest of the chain, due to fewer numbers of couplings with neighbouring spins. Thus, there exist a time $t_1$ when the state of the end-spins is still mainly $\sigma_x$, whereas the rest of the spins have evolved to many-body correlations. A second $\pi/2$ pulse brings the end-spin magnetization back to the longitudinal axis, while an appropriate phase cycling scheme cancels out other terms, thus obtaining the state

$$\delta\rho_{end} = \delta\rho_z^1 + \delta\rho_z^N. \tag{28}$$

We note that the chain geometry prevents breaking the symmetry between spin 1 and $N$. Here the phase cycling achieves a similar result of temporal averaging in the preparation of pseudo-pure states. The sequence that prepares this state can thus be written as

$$\left.\frac{\pi}{2}\right|_\alpha - t_1 - \left.\frac{\pi}{2}\right|_{-\alpha}, \tag{S1}$$

with $\alpha = \{-x, y\}$, to average out terms that do not commute with the total magnetization $\Sigma_z$. As the phase cycling does not cancel zero-quantum coherences, they will be the main source of errors in the initialization scheme [12, 118].

A similar control strategy can be as well used to read out the spins at the end of the chain even if the observable in inductively measured NMR is the collective magnetization of the spin ensemble, $\Sigma_z$. To measure a different observable, the desired state must be prepared prior to acquisition. Thus we want to turn $\Sigma_z$ into the

end-chain state, Eq. (28). In general, the sequence used for readout cannot be a simple inversion of the end-selection step since this is not a unitary –reversible– operation. It is however sufficient to ensure that the state prior to the end-selection sequence has contributions mainly from population terms ($\propto \sigma_z^k$) for the sequence (S1) to work as a readout step. A two-step phase cycling [63] is enough to select populations and zero quantum terms, which in turn can be eliminated by purging pulses [160]. However, since the states created by evolution under the DQ Hamiltonian are already of the form $\propto \sigma_z^k$, the (S1) sequence with a two-step phase cycling is enough for the end-readout step.

The initialization technique described above was first introduced in [12] (see also [118, 161]); Kaur [134] later demonstrated both the initialization and readout techniques in a pure, single crystal of FAp grown by the flux method [125] and placed in a 7 T wide-bore magnet with a 300 MHz Bruker Avance Spectrometer and a probe tuned to 282.4 MHz for $^{19}$F measurement. The effectiveness of the initialization and readout methods was verified by probing the transport dynamics, as driven by the DQ Hamiltonian, comparing the end-polarized states and observables with the thermal-equilibrium state. To this goal, the collective or end-chain magnetization was measured as the evolution time was increased under the DQ Hamiltonian. The 8-pulse sequence [78] in Fig. 7 was used to implement the DQ Hamiltonian with a $1.45\mu$s $\pi/2$ pulse length. The evolution time was incremented by varying the inter-pulse delay from $1\mu$s to $6.2\mu$s and repeating the sequence from 1 to 12 times. The evolution was restricted to a timescale where the ideal model applies and errors arising from discrepancies from the ideal model (leakage to other chains and next-nearest neighbor couplings) are small [118]. In this timescale, the initial perturbation travels across $\approx 17$ spins [119], however only polarization leaving one end of the chain could be observed: a clear signature of the polarization reaching the other end is erased by the distribution of chain lengths. Still, the experimental verification of initial state preparation is possible even at these short time scales thanks to marked differences in the signal arising from the evolution of thermal and end-polarized state under DQ Hamiltonian.

Figure (10) (blue) shows the observed evolution of the collective magnetization $\Sigma_z$ under the DQ Hamiltonian, starting from the thermal initial state, $\delta\rho_{th} = \Sigma_z$; the signal is given by $S^{th}(t) \propto \mathrm{Tr}\left\{U_{MQ}\delta\rho_{th}U_{MQ}^{\dagger}\Sigma_z\right\}$, with $U_{MQ}(t) = e^{-i\mathcal{H}_{DQ}t}$. Modelling the physical spin system by an ensemble of equivalent and independent spin chains with nearest-neighbour couplings only, we can derive analytical formulas for the evolution to fit the experimental data. Under this approximation, the DQ Hamiltonian is exactly solvable by invoking a Jordan-Wigner mapping onto a system of free fermions [149, 162]. The analytical solution for the evolution of the thermal state, when measuring the collective magnetization, is given by [119, 134]:

$$S^{th}(t) = \sum_{p=1}^{N} f_{p,p}(2t), \qquad (29)$$

with

$$f_{j,q}(t) = \sum_{m=0}^{\infty}[i^{mv+\delta}J_{mv+\delta}(2bt) - i^{mv+\sigma}J_{mv+\sigma}(2bt)]$$
$$+ \sum_{m=1}^{\infty}[i^{mv-\delta}J_{mv-\delta}(2bt) - i^{mv-\sigma}J_{mv-\sigma}(2bt)], \tag{30}$$

where $v = 2(N+1), \delta = q - j, \sigma = q + j$ and $J_n$ are the $n^{th}$ order Bessel functions of the first kind. The data points in Fig. (10) were fitted to this analytical function (Eq. 29).

The red data in figure (10) show the evolution of the end polarized initial state under the DQ-Hamiltonian, measured using the readout strategies outlined above, $S^{sre} \propto \mathrm{Tr}\left\{U_{MQ}\delta\rho_{end}U_{MQ}^{\dagger}\delta\rho_{end}\right\}$. The fitting function used is given by

$$S^{sre}(t) = f_{1,1}^2(t) + f_{1,N}^2(t), \tag{31}$$

which has the same form as the transport of a single excitation in a pure state chain [97, 101], $|\langle 1_N|U_{xx}(t)|1_1\rangle|$. This experiment is thus a direct simulation of quantum state transport.

To further validate the initialization and readout method, in figure (11) (blue, open circles) we plot the system dynamics when starting from an end-polarized state, Eq. (28) (where polarization is localized at the ends of the chain) and reading out the collective magnetization, $S^{se} \propto \mathrm{Tr}\left\{U_{MQ}\delta\rho_{end}U_{MQ}^{\dagger}\Sigma_z\right\}$. The red (filled circle) data in Fig. (11) shows a complementary measurement where we start from thermal initial state, given by the collective magnetization, and read out the ends of the chains after evolution under the DQ Hamiltonian, $S^{re} \propto \mathrm{Tr}\left\{U_{MQ}\delta\rho_{th}U_{MQ}^{\dagger}\delta\rho_{end}\right\}$. Both these data sets were fitted by the analytical expression
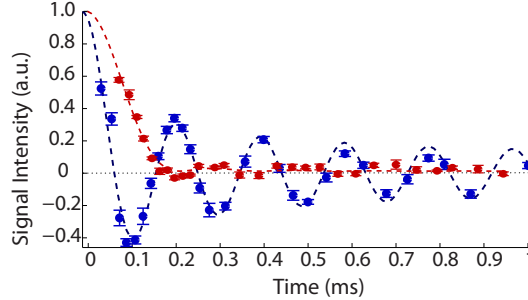


**Fig. 10** Transport under the DQ Hamiltonian, first reported in [134]. Blue: Initial state $\delta\rho_{th}$; readout, collective magnetization, $\Sigma_z$. Red: Initial state, $\delta\rho_{end}$; readout, end readout. Data points are the experimental data (Blue: collective magnetization; Red end of chain magnetization), with error bars obtained from the offset of the signal from zero. The measurement was done using a single scan (blue) and 4 scans (red) as required by using twice the two-step phase cycling of sequence S1. The lines are the fits using the analytical model. The fitting gives the following values for the dipolar coupling: 8.165 (blue, thermal state), and 8.63 (red) $\times 10^3$rad/s. The two curves highlight the differences arising from the different initial state and readouts.
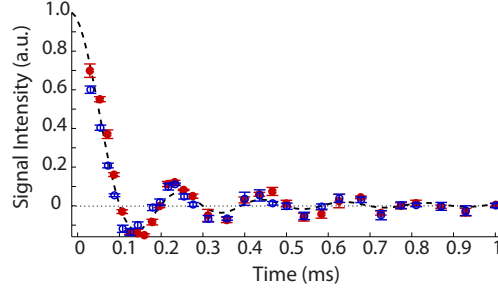
**Fig. 11** Evolution under the DQ Hamiltonian, first reported in [134]. Blue, open circles: Initial state, $\delta\rho_{end}$; readout, collective magnetization, $\Sigma_z$. Red, filled circles: Initial state, $\delta\rho_{th}$; readout, end-spin readout. Data points are the experimental data (Blue: collective magnetization; Red end of chain magnetization). Error bars are given by the offset of the signal from zero. The measurement was done using 2 scans as required by the two step phase cycling in sequence S1. The lines are the fits using the analytical model. The fitting gives the following values for the dipolar coupling: 8.172 (blue) and $8.048 \times 10^3$ rad/s (red). The experimental data shows remarkable agreement between the two schemes, thus confirming the validity of the initialization and readout methods.

$$S^{se}(t) = S^{re}(t) = \sum_{p=1}^{N} f_{1,p}^2(t), \tag{32}$$

As it is evident from the near perfect fitting, the analytical model explains the experimental data quite precisely.

Figures (10) and (11) show very different chain dynamics for the two initial states (with and without end selection), giving an experimental validation of our initialization method. Furthermore, the data and fittings for end selection and end readout measurements, Fig. (11), are very similar. This indicates the robustness of the readout step.

The small discrepancy in the fitting parameter (coupling strength) in the spin transport experiment (Fig. 10, red data) is due to accumulation of imperfections of the end-select and readout schemes. Unfortunately, the phase cycling scheme does not cancel out zero-quantum terms. Thus, residual polarization on spins 2 and N-1 $(\sigma_z^2 + \sigma_z^{N-1})$ and correlated states of the form $\sigma_j^z(\sigma_{j-1}^+\sigma_{j+1}^- + \sigma_{j-1}^-\sigma_{j+1}^+)$ lower the fidelity with the desired state. This effect is more important for the last experiment, since not only errors in the two selection steps accumulate but the readout step is further degraded by the fact that it is not applied to the ideal state expected after transport. Still, the agreement of the experimental data with the analytical model indicates that these errors are small and do not invalidate the scheme.

The end-selection scheme presented above can not only prepare the end-chain polarized states, but also the logical states –introduced in Eq. (27)– required for quantum information transport. First we prepare the end polarized state $\delta\rho_{end}$ by the sequence (S1). Then this evolves under the DQ Hamiltonian for a very short time $t_{DQ} = 14.7 \mu s$, thus creating a two-spin correlated state as required. We can write this initialization sequence as

$$\left.\frac{\pi}{2}\right|_{\alpha} - t_1 - \left.\frac{\pi}{2}\right|_{\beta} - \text{DQ}^{\gamma}, \tag{S2}$$

where $\text{DQ}^{\gamma=x}$ is propagation under $U_{MQ}(t_{\text{DQ}}) = e^{-i\overline{\mathcal{H}}_{DQ}t_{DQ}}$ and $\text{DQ}^{\gamma=y}$ under $U_{MQ}^{\dagger}$. Setting $[\alpha, \beta, \gamma] = [-x, x, x]$, the state after the sequence (S2) is approximately given by zero and double quantum coherences, $\delta\rho_{end}(t_{\text{DQ}}) \approx \sigma_{1,2}^{\text{zq}} + \sigma_{n-1,n}^{\text{zq}} + \sigma_{1,2}^{\text{DQ}} + \sigma_{n-1,n}^{\text{DQ}}$, where $\sigma_{i,j}^{\text{zq}} = (\sigma_x^i\sigma_y^j - \sigma_y^i\sigma_x^j)$ and $\sigma_{i,j}^{\text{DQ}} = (\sigma_x^i\sigma_y^j + \sigma_y^i\sigma_x^j)$. A double quantum filter given by the four-step phase cycling scheme,

$$[\alpha, \beta, \gamma] = \{[-x, x, x]; [y, -y, x]; [-x, -x, y]; 1[y, y, y]\}$$

cancels out the zero-quantum terms and selects the double-quantum terms, which is our desired state: $\delta\rho_y^L \propto \sigma_{1,2}^{\text{DQ}} + \sigma_{n-1,n}^{\text{DQ}}$. Figure (12) shows the evolution of this state under the DQ Hamiltonian. We note that this experiment implements the transport of quantum information via a maximally mixed quantum channel. The dynamics was monitored by measuring the collective magnetization, $S^L \propto \text{Tr}\left\{U_{MQ}\delta\rho_y^L U_{MQ}^{\dagger}\sigma_z\right\}$. The data points were fitted by the expression

$$S^{yL}(t) = f_{1,2}(2t) + f_{N-1,N}(2t), \tag{33}$$

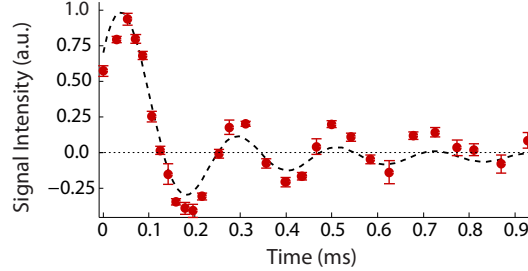showing good agreement with the analytical model.



**Fig. 12** Evolution of the logical state $\delta\rho_y^L$ (Eq. 27) under the transport Hamiltonian, first reported in [134]. The logical initial state was prepared using the sequence (S2) and its evolution under the DQ Hamiltonian monitored by observing the collective magnetization. Circles represent the experimental data and the dahshed line is the fit to the analytical model of Eq. (33). The fitting of the data points gives a dipolar coupling value of $7.551 \times 10^3$ rad/s.

### 3.2.5 Experimental insight into transport dynamics

Implementing experimentally quantum state transfer, even with the constraints described above regarding state initialization and readout, is critical to further learn about practical features and limitations that do not arise in the idealized model. It is thus possible to gather further insight into the transport dynamics, for example

by studying more in depth the state created during transport [119, 134] and its decay [140, 163]. In addition it is possible to explore the effects that discrepancies from the ideal model, such as longer-range couplings and couplings to external spins, have on transport [118]. These phenomena often go beyond analytical solutions and are thus best explored experimentally.

**Multiple quantum coherence dynamics –** To gather further insight into the transport dynamics it would be interesting to completely characterize the evolved state, as it is done in state tomography [164]. Unfortunately, given the large dimension of the system considered and measurement constraints, this is not possible. We can still infer more information on the state by measuring not only the system's polarization (either collective polarization, $\Sigma_z$ or the end-spin polarization, $\delta\rho_{end}$) but also spin correlations encoded in multiple quantum coherences. As these MQC intensities present a beating every time the polarization is transferred from spin 1 to spin $N$, it would be possible in principle to monitor state transfer driven by the DQ Hamiltonian by measuring the MQC intensities, which are more easily detected [11]. Although this signature is washed out by a distribution of chain lengths [118], MQC intensities still retain information about the state that is transported, for example distinguishing between the thermal and end-polarized state, as shown in Figure (13).
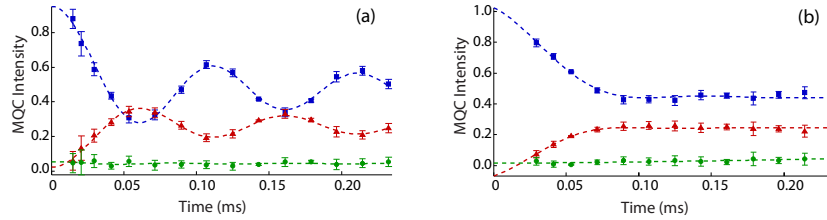


**Fig. 13** Evolution of multiple quantum coherences $I'_n(t)$ (0Q blue squares, 2Q red triangles, 4Q green circles) first reported in [134]: (a) Initial state: $\delta\rho_{th}$. Readout: collective magnetization. (b) Initial state: $\delta\rho_{end}$ Readout: end-readout. Data points are the experimental data (collective magnetization in (a) and end of chain magnetization in (b)). The measurement was done using a single scan in (a) and 4 scans in (b) for the four step phase cycling. The error bars are estimated from the deviation of 1st order quantum coherence from zero. The first two data points were measured using a 4 pulse sequence to implement the DQ Hamiltonian (instead of a standard 8 pulse sequence), leading to greater error bars. The data points are fitted by analytical functions (blue and red lines) obtained from the DQ Hamiltonian with NN couplings [equations (35) and (36) for figures (a) and (b) respectively]. The 4Q coherences (which should be zero in the ideal model) were simply fitted with a constant. Fitting of the data gives dipolar coupling: 7.971 (a) and 8.492 (b) $\times 10^3$rad/s.

The figure shows the evolution of the MQC intensities experimentally measured for different initial states and readouts. Here the signal is slightly different than what presented in Eq. (12). When the initial state $\rho_i$ and observable $\rho_{obs}$ are different, the signal $S^{obs}_{\varphi_m} = \text{Tr}\left\{\rho_f^m(t)\rho_{obs}\right\}$ yields the coherence order intensity

$$I'_q(t) = \sum_{m=1}^{M} S_{\varphi_m}(t) e^{-iq\varphi_m} = \mathrm{Tr}\left\{\rho_i(t)^q \rho_{obs}(t)^{-q} + \rho_i(t)^{-q} \rho_{obs}(t)^q\right\}, \quad (34)$$

where $\rho_i(t) = U_{MQ}\rho_i U^\dagger_{MQ}$ and $\rho_{obs}(t) = U_{MQ}\rho_{obs}U^\dagger_{MQ}$. Fig. 13(a) shows the usual MQC signal, obtained by measuring the collective magnetization and starting from an initial thermal state (Eq. 4). The data points are fitted by the functions predicted by the analytic model [11, 148, 162]:

$$
\begin{aligned}
J_0^{th}(t) &= \frac{1}{N} \sum_k \cos^2[4bt\cos(\psi_k)], \\
J_2^{th}(t) &= \frac{1}{2N} \sum_k \sin^2[4bt\cos(\psi_k)],
\end{aligned}
\quad (35)
$$

where $N$ is the number of spins in the chain and $\psi_k = k\pi/(N+1)$.

The data for the case where we initialize the ends of the chains before letting the system evolve under DQ Hamiltonian and then read out the ends is shown in Fig. 13(b). The data is fitted to the normalized MQC intensities given by the analytical model [11]:

$$
\begin{aligned}
J_0^{sre}(t) &= \frac{4}{(N+1)^2} \sum_{k,h} \sin^2(\kappa)\sin^2(\eta)\cos^2(\psi_k+\psi_h)(1+\cos[(N+1)\kappa]\cos[(N+1)\eta]), \\
J_2^{sre}(t) &= \frac{2}{(N+1)^2} \sum_{k,h} \sin^2(\kappa)\sin^2(\eta)\sin^2(\psi_k+\psi_h)(1+\cos[(N+1)\kappa]\cos[(N+1)\eta]).
\end{aligned}
$$
$$(36)$$

The fitting yielded a dipolar coupling strength b=$8.492\times10^3$ rad/s [134], a slightly higher value than what is obtained from other independent experiments on the same system. As mentioned, this is due to accumulation of errors in the initialization and readout steps.

MQC intensities provide further insight into the dynamics of various initial states driven by the transport Hamiltonian. In particular, these experiments yield an independent validation of the initialization and readout steps. Unfortunately, MQC are not enough to fully reconstruct the system's state. For example, during the course of the evolution, multi-spin correlations are created [119], as the polarization wavepacket spreads out. This effects is due to the fact that for a Hamiltonian with all-equal coupling transport is eventually dispersive [165]. In order to reach perfect state transfer one needs to study alternative strategies, including static [97, 101] or dynamic [85, 105] engineering of optimal couplings or a weakening of the coupling between the bulk spins and the end-chain spins [152, 166–169]. Still, it would be interesting to study the sequential growth of multi-spin correlations in the case of equal-coupling Hamiltonians, not only to characterize the dynamics but also to further study the decay of these correlations [140], which might be faster than for single-spin states [170, 171].

Ramanathan *et al.* [119] experimentally characterized the sequential growth of multi-spin correlations using an x-basis encoding of MQC [147]. In standard MQC experiments, as explained in Section 2.2, we encode the coherence order with respect to $\Sigma_z$ eigenstates. The encoding is simply obtained by the phase shift acquired

during a collective rotation of the spins about the z-axis. Similarly, a collective rotation about the x-axis results in an encoding of MQC with respect to eigenstates of $\Sigma_x = \sum_k \sigma_x^k$. Higher order coherences in the x-basis are a signature of the presence of multi-spin correlations [147]. It was observed (see figure (4) in [119]) that during the evolution under the DQ Hamiltonian, in a one-dimensional system after the initial rapid creation of 3-spin correlations (and concomitant reduction in the single spin term), the coherence orders change quite slowly. This confirms that although the equal-coupling DQ Hamiltonian is dispersive, the rate of dispersion is quite slow, thus one can still achieve high fidelity transport over short distances.

**Errors and decoherence –** The greatest contribution of experimental implementations of QST, even in systems with practical limitations, for example not allowing scalability, is in the study of effects that go beyond the ideal analytic models. Indeed, while transport in the one-excitation manifold (and its generalization to mixed states) via local Hamiltonian can be either solved analytically or efficiently simulated on a classical computer, more realistic models, closer to possible physical implementations, in general cannot be solved. Thus it becomes interesting to simulate experimentally possible discrepancies of a real system from the ideal model, as many of these effects will be common to many different physical systems. These include long-range couplings inside the chain and interaction of the chain spins with an environment and possibly with other nearby chains, as it would happen in a distributed quantum computing architecture.

Using fluorapatite as a model system, W. Zhang and coworkers [118] examined how the ideal model (an isolated spin chain, with a nearest-neighbor only DQ Hamiltonian) compares to the physical system's evolution. They used both experimental and numerical methods to break down the various contributions to the observed deviation from the ideal model. In addition to errors introduced in state initialization, that we mentioned above, they analyzed experimental errors introduced during the DQ Hamiltonian engineering as well as by the presence of longer-range couplings, both within a single chain and between adjacent spin chains, and by a distribution of chain lengths.

It was found that pulse errors were the main cause of the deviation of the engineered Hamiltonian (via the sequence in Fig. 7) from the ideal DQ Hamiltonian, Eq. (19), while the experimental implementation of the sequence is enough to reduce the effects of second-order terms in AHT. Despite the experimental Hamiltonian is not ideal, the effects are only felt at long times, much longer than usually explored during transport experiments and thus it is not a limitation for studying transport over 10-20 spins (we note that the fidelity of transport would decrease sensibly for longer chains even in the ideal model with equal couplings).

A larger contribution to the deviation of the experimental signal from the expected ideal behavior over the timescale of interest was due to long-range couplings. The main results were the creation of spurious terms in the evolved state, as signaled by the appearance of four-quantum coherences, which are not expected in the ideal model, and a decay of the signal toward its long-time average value (that is, a damping of its coherent oscillation amplitude). It was found that the effects of in-chain couplings were hardly distinguishable from cross-chain couplings, even

if they have different strengths, since six neighboring chains contribute to the second effect. These results are important for the experimental implementation of QST in any physical platform, as they indicate that much attention should be paid not only to isolating the chain from the environment and other nearby spin wires, but also to carefully engineer the transport Hamiltonian, for example by filtering out next-nearest neighbor couplings [85] that would otherwise decrease the transport fidelity [154].

## 4 Conclusions and outlook

NMR systems and techniques have provided a fertile platform for experimental investigation of quantum state transfer in spin chains. From the first observation of polarization transfer, predating the formal definition QST [10], to the realization of QST simulations in small molecules and in larger solid-state spin systems, the experiments have drawn on the strength of NMR, in particular on its long history of well-developed control techniques. Thus, NMR implementations have been invaluable both as proof-of-principle demonstrations of QST protocols and to explore dynamics occurring in real systems that go beyond what can be analytically solved or numerically simulated.

Some challenges and limitations of NMR-based implementations of QST remain. On the one side, liquid-state implementations have been limited in size by the number of spins in the molecules. Although larger molecules exist, a more fundamental challenge derives from the difficulty of controlling the natural Hamiltonian in larger systems in order to obtain the desired transport interaction. In addition, the weakness of the scalar couplings makes transport in liquid-state molecules a slow process that quickly competes with decoherence. Still, liquid-state implementations might be well-suited to demonstrate control-intensive protocols, to refine the control techniques that will be as well required in larger systems and to study the effects of limitations and constraints in the control.

QST in larger systems and at a faster rate has been obtained using solid-state NMR. However, in these systems the constraints imposed by collective control and by ensemble measurements have prevented the experimental characterization of transport fidelity: indeed, due to the chain length distribution, the signal averaged over the chain ensemble does not provide information about the transport fidelity. Using different systems, for example $^1$H doped FAp (or $^{19}$F-doped HAp), combined with control techniques could provide a solution to this problem [134].

Both traditional liquid- and solid-state NMR systems are not well suited to move beyond simple demonstrations of QST and toward its actual implementation in the context of a QIP architecture. Still, the techniques and insight developed on these systems can help the design of potentially scalable systems. For example, NMR techniques could be used in hybrid systems, comprising electronic and nuclear spins or combining magnetic resonance and optical techniques for initialization and readout.

A spin-based distributed quantum information processor can be based on single-crystal molecular monolayers as proposed in [19, 172]. The individual registers are organic molecules with a localized free-radical electron spin, which interacts with a small number of nuclear spins via an anisotropic hyperfine interaction [100]. These molecules can be made into single-crystal molecular monolayers using either a Langmuir-Blodgett process [173], or by self-assembly [174]. This system could be used to explore QST or, conversely, using some of the registers to form a wire could enable building larger architectures based on this model.

Another system that has emerged as a potential candidate for QIP architectures is the Nitrogen-Vacancy (NV) center in diamond [9], thanks to its long coherence times and the possibility of optical initialization and readout even at room temperature. The NV center could be thus at the center of small quantum registers [175, 176], where nuclear spins play the role of long-time storage qubits with fast access and control provided by the NV electronic spin. To connect the registers, other spins in the diamond lattice could be used, for example Nitrogen electronic spins [101, 177, 178]. While Nitrogen implantation can be done with improving precision [179–182], the Nitrogen to NV conversion is limited, as vacancies need to recombine with single Nitrogens by annealing at high temperature. Thus although it is difficult to envision regular NV spin chains, the nitrogen defects (P1 centers [183]) are electronic spin-1/2 that can be used as quantum wires to connect the NV-center qubits. While NV centers can be initialized to their ground state and controlled individually by a combination of microwave and optical control [184], the P1 can only be controlled collectively and are found in their thermal (highly mixed) state. Using the P1 centers as quantum wires would enable larger separation between NV qubits and thus their individual addressing by sub-diffraction-limit optical techniques [184, 185]. Local operations at the NV center register would allow for quantum error correction and entanglement purification, with the potential of a fault-tolerant, room temperature quantum computer. The P1 centers interact via the dipolar interaction, which can be truncated to its secular part [101], Eq. (6), at high enough magnetic fields or even reduced to an Ising Hamiltonian thanks to gradients [177]. The transport Hamiltonian (either DQ or XX Hamiltonian) can then be engineered via the multiple-pulse techniques discussed in this chapter, while magnetic resonance control techniques can help in obtaining the desired couplings of the NV centers to the P1 spins (to achieve for example, the weak-coupling regime [152, 166–169, 186, 187]). While dephasing noise limits the transport fidelity [178] material engineering and dynamical decoupling techniques that can increase the coherence time [188, 189] by orders of magnitude might make this scheme practical.

Alternatively, the NV centers could be used as single-spin detectors [190–192] to read out spins in various solid-state systems, either as a scanning head or as a substrate of surface spin networks [172, 193]. This would allow transforming some spin systems, which currently lack addressability, into potential candidate platforms for scalable QIP and in particular for QST. Combining local addressability with strong gradients can enable Hamiltonian engineering, inspired by NMR

multiple-pulse control techniques [82], which allow state transfer in more general networks [85, 105].

From the examples we briefly discussed it follows that, as it is a long tradition in QIP, magnetic resonance techniques will continue to play an important role in advancing the experimental implementations of quantum state transfer.

# References

1. S. Bose, Phys. Rev. Lett. **91**(20), 207901 (2003)
2. M. Mariantoni, H. Wang, T. Yamamoto, M. Neeley, R.C. Bialczak, Y. Chen, M. Lenander, E. Lucero, A.D. O'Connell, D. Sank, M. Weides, J. Wenner, Y. Yin, J. Zhao, A.N. Korotkov, A.N. Cleland, J.M. Martinis, Science **334**(6052), 61 (2011)
3. D. Loss, D.P. DiVincenzo, Phys. Rev. A **57**(1), 120 (1998)
4. X. Li, Y. Wu, D. Steel, D. Gammon, T.H. Stievater, D.S. Katzer, D. Park, C. Piermarocchi, L.J. Sham, Science **301**(5634), 809 (2003)
5. G. Ciaramicoli, I. Marzoli, P. Tombesi, Phys. Rev. A **75**, 032348 (2007)
6. L.M. Duan, E. Demler, M.D. Lukin, Phys. Rev. Lett. **91**(9), 090402 (2003)
7. J. Simon, W.S. Bakr, R. Ma, M.E. Tai, P.M. Preiss, M. Greiner, Nature **472**(7343), 307 (2011)
8. B.E. Kane, Nature **393**, 133 (1998)
9. J. Wrachtrup, F. Jelezko, J. Phys.: Condens. Matter **18**(21), S807 (2006)
10. Z. Madi, B. Brutscher, T. Schulte-Herbruggen, R. Bruschweiler, R. Ernst, Chem. Phys. Lett. **268**(3), 300 (1997)
11. P. Cappellaro, C. Ramanathan, D.G. Cory, Phys. Rev. Lett. **99**(25), 250506 (2007)
12. P. Cappellaro, C. Ramanathan, D.G. Cory, Phys. Rev. A **76**(3), 032317 (2007)
13. J. Zhang, X. Peng, D. Suter, Phys. Rev. A **73**, 062325 (2006)
14. D.D. Traficante, Concepts in Magnetic Resonance **3**(1), 49 (1991)
15. N. Bloembergen, Physica **15**, 386 (1949)
16. A. Abragam, M. Goldman, Reports on Progress in Physics **41**(3), 395 (1978)
17. C. Ramanathan, App. Mag. Res. **34**(3), 409 (2008)
18. T.D. Ladd, J.R. Goldman, F. Yamaguchi, Y. Yamamoto, E. Abe, K.M. Itoh, Phys. Rev. Lett. **89**(1), 017901 (2002)
19. D. Cory, R. Laflamme, E. Knill, L. Viola, T. Havel, N. Boulant, G. Boutis, E. Fortunato, S. Lloyd, R. Martinez, C. Negrevergne, M. Pravia, Y. Sharf, G. Teklemariam, Y. Weinstein, W. Zurek, Fort. der Phys. **48**(9-11), 875 (2000)
20. B. Criger, G. Passante, D. Park, R. Laflamme, Phil. Trans. R. Soc. A **370**(1976), 4620 (2012)
21. C. Ramanathan, N. Boulant, Z. Chen, D.G. Cory, I. Chuang, M. Steffen, Quantum Information Processing **3**, 15 (2004)
22. J.A. Jones, Progress in Nuclear Magnetic Resonance Spectroscopy **59**(2), 91 (2011)
23. C. Negrevergne, T.S. Mahesh, C.A. Ryan, M. Ditty, F. Cyr-Racine, W. Power, N. Boulant, T. Havel, D.G. Cory, R. Laflamme, Phys. Rev. Lett. **96**(17), 170501 (2006)
24. A. Abragam, *Principles of Nuclear Magnetism* (Oxford Univ. Press, 1961)
25. R. Ernst, G. Bodenhausen, A. Wokaun, *Principles of nuclear magnetic resonance in one and two dimensions* (Clarendon Press Oxford, 1987)
26. C.P. Slichter, *Principles of Magnetic Resonance*, 3rd edn. (Springer-Verlag, 1996)

27. P.T. Callaghan, *Principles of Nuclear Magnetic Resonance Microscopy* (Oxford Science Publications, 1991)
28. M.H. Levitt, Prog. Nucl. Mag. Res. Spect. **18**(2), 61 (1986)
29. E.M. Fortunato, M.A. Pravia, N. Boulant, G. Teklemariam, T.F. Havel, D.G. Cory, J. Chem. Phys. **116**, 7599 (2002)
30. M.A. Pravia, N. Boulant, J. Emerson, A. Farid, E.M. Fortunato, T.F. Havel, R. Martinez, D.G. Cory, J. Chem. Phys. **119**, 9993 (2003)
31. N. Khaneja, T. Reiss, C. Kehlet, T. Schulte-Herbuggen, S. Glaser, J. Magn. Res. **172**, 296 (2005)
32. J. Zhang, G.L. Long, W. Zhang, Z. Deng, W. Liu, Z. Lu, Phys. Rev. A **72**, 012331 (2005)
33. D.G. Cory, A.F. Fahmy, T.F. Havel, Proc. Nat. Acad. Sc. **94**(5), 1634 (1997)
34. N.A. Gershenfeld, I.L. Chuang, Science **275**(5298), 350 (1997)
35. D. Deutsch, Proc. R. Soc. A **400**(1818), 97 (1985)
36. J.A. Jones, M. Mosca, J. Chem. Phys. **109**(5), 1648 (1998)
37. M.S. Anwar, J.A. Jones, D. Blazina, S.B. Duckett, H.A. Carteret, Phys. Rev. A **70**, 032324 (2004)
38. I.L. Chuang, L.M.K. Vandersypen, X. Zhou, D.W. Leung, S. Lloyd, Nature **393**(6681), 143 (1998)
39. R. Cleve, A. Ekert, C. Macchiavello, M. Mosca, Proceedings of the Royal Society of London. Series A: Mathematical, Physical and Engineering Sciences **454**(1969), 339 (1998)
40. M. Kawamura, T. Morimoto, T. Kumaya, R. Sawae, K. Takarabe, Y. Manmoto, Int. J. Quant. Chem. **105**(6), 750 (2005)
41. N. Linden, H. Barjat, R. Freeman, Chemical Physics Letters **296**(1-2), 61 (1998)
42. L. Grover, in *Proceedings of 28th Annual ACM Symposium on Theory of Computing (STOC)* (1996), pp. 212–219
43. J.A. Jones, M. Mosca, R.H. Hansen, Nature **393**(6683), 344 (1998)
44. I.L. Chuang, N. Gershenfeld, M. Kubinec, Phys. Rev. Lett. **80**, 3408 (1998)
45. C.S. Yannoni, M.H. Sherwood, D.C. Miller, I.L. Chuang, L.M.K. Vandersypen, M.G. Kubinec, Applied Physics Letters **75**(22), 3563 (1999)
46. Y. Weinstein, T. Havel, J. Emerson, N. Boulant, M. Saraceno, S. Lloyd, D.G. Cory, J. Chem. Phys. **121**, 6117 (2004)
47. L. Vandersypen, M. Steffen, G. Breyta, C. Yannoni, M. Sherwood, I. Chuang, Nature **414**, 883 (2001)
48. S.S. Somaroo, C.H. Tseng, T.F. Havel, R. Laflamme, D.G. Cory, Phys. Rev. Lett. **82**, 5381 (1999)
49. C.H. Tseng, S. Somaroo, Y. Sharf, E. Knill, R. Laflamme, T.F. Havel, D.G. Cory, Phys. Rev. A **61**, 012302 (1999)
50. J. Du, N. Xu, X. Peng, P. Wang, S. Wu, D. Lu, prl **104**, 030502 (2010)
51. C.A. Ryan, M. Laforest, J.C. Boileau, R. Laflamme, Phys. Rev. A **72**, 062317 (2005)
52. J. Du, H. Li, X. Xu, M. Shi, J. Wu, X. Zhou, R. Han, Phys. Rev. Lett. **88**, 137902 (2002)
53. A. Mitra, K. Sivapriya, A. Kumar, J. Mag. Res. **187**(2), 306 (2007)
54. Y.S. Weinstein, S. Lloyd, J. Emerson, D.G. Cory, Phys. Rev. Lett. **89**, 157902 (2002)
55. D.G. Cory, M.D. Price, W. Maas, E. Knill, R. Laflamme, W.H. Zurek, T.F. Havel, S.S. Somaroo, Phys. Rev. Lett. **81**(10), 2152 (1998)
56. L. Viola, E.M. Fortunato, M.A. Pravia, E. Knill, R. Laflamme, D.G. Cory, Science **293**(5537), 2059 (2001)
57. E.M. Fortunato, L. Viola, J. Hodges, G. Teklemariam, D.G. Cory, New J. Phys. **4**(1), 5 (2002)
58. N. Boulant, L. Viola, E.M. Fortunato, D.G. Cory, Phys. Rev. Lett. **94**, 130501 (2005)
59. P. Cappellaro, J.S. Hodges, T.F. Havel, D.G. Cory, J. Chem. Phys. **125**, 044514 (2006)
60. J.S. Hodges, P. Cappellaro, T.F. Havel, R. Martinez, D.G. Cory, Phys. Rev. A **75**(4), 042320 (2007)
61. P. Cappellaro, J.S. Hodges, T.F. Havel, D.G. Cory, Phys. Rev. A **75**, 042321 (2007)
62. E. Knill, I. Chuang, R. Laflamme, Phys. Rev. A **57**(5), 3348 (1998)
63. G. Bodenhausen, H. Kogler, R. Ernst, J. Mag. Res. **58**(3), 370 (1984)

64. J. Keeler, *Understanding NMR Spectroscopy* (John Wiley & Sons, 2010)
65. J. Baum, R. Tycko, A. Pines, Phys. Rev. A **32**, 3435 (1985)
66. R. Freeman, Progress in Nuclear Magnetic Resonance Spectroscopy **32**(1), 59 (1998)
67. C.A. Ryan, C. Negrevergne, M. Laforest, E. Knill, R. Laflamme, Phys. Rev. A **78**(1), 012328 (2008)
68. V.F. Krotov, *Global methods in optimal control theory* (Marcel Dekker, Inc. New York, 1996)
69. L. Viola, S. Lloyd, Phys. Rev. A **58**, 2733 (1998)
70. K. Khodjasteh, D.A. Lidar, Phys. Rev. Lett. **95**(18), 180501 (2005)
71. G.S. Uhrig, Phys. Rev. Lett. **98**(10), 100504 (2007)
72. E.L. Hahn, Phys. Rev. **80**(4), 580 (1950)
73. H.Y. Carr, E.M. Purcell, Phys. Rev. **94**(3), 630 (1954)
74. S. Meiboom, D. Gill, Rev. Sc. Instr. **29**(8), 688 (1958)
75. N. Bloembergen, R.V. Pound, Phys. Rev. **95**, 8 (1954)
76. W. Zhang, D.G. Cory, Phys. Rev. Lett. **80**, 1324 (1998)
77. G.S. Boutis, P. Cappellaro, H. Cho, C. Ramanathan, D.G. Cory, J. Mag. Res. **161**, 132 (2003)
78. Y.S. Yen, A. Pines, J. Chem. Phys. **78**(6), 3579 (1983)
79. M. Munowitz, A. Pines, *Principle and Applications of Multiple-Quantum NMR*, *Adv. Chem. Phys.*, vol. 66 (John Wiley & Sons, Inc., 1987)
80. M. Munowitz, A. Pines, M. Mehring, J. Chem. Phys. **86**(6), 3172 (1987)
81. J. Waugh, L. Huber, U. Haeberlen, Phys. Rev. Lett. **20**, 180 (1968)
82. U. Haeberlen, *High Resolution NMR in Solids: Selective Averaging* (Academic Press Inc., New York, 1976)
83. U. Haeberlen, J. Waugh, Phys. Rev. **175**(2), 453 (1968)
84. W.K. Rhim, D.D. Elleman, K.U. Schreiber, R.W. Vaughan, J. Chem. Phys. **60**, 4595 (1974)
85. A. Ajoy, P. Cappellaro, ArXiv:1208.3656 (2012)
86. S. Schirmer, in *Lagrangian and Hamiltonian Methods for Nonlinear Control 2006*, *Lecture Notes in Control and Information Sciences*, vol. 366 (Springer, 2007), pp. 293–304
87. J. Zhang, M. Ditty, D. Burgarth, C.A. Ryan, C.M. Chandrashekar, M. Laforest, O. Moussa, J. Baugh, R. Laflamme, Phys. Rev. A **80**, 012316 (2009)
88. M.A. Nielsen, I.L. Chuang, *Quantum computation and quantum information* (Cambridge University Press, Cambridge; New York, 2000)
89. J. Zhang, K.B. Whaley, Phys. Rev. A **71**(5), 052317 (2005)
90. P. Cappellaro, J. Emerson, N. Boulant, C. Ramanathan, S. Lloyd, D.G. Cory, Phys. Rev. Lett. **94**, 020502 (2005)
91. J.S. Lee, A.K. Khitrin, J. Chem. Phys. **121**(9), 3949 (2004)
92. J.S. Lee, A.K. Khitrin, Phys. Rev. A **71**, 062338 (2005)
93. J.S. Lee, T. Adams, A.K. Khitrin, New J. Phys. **9**(4), 83 (2007)
94. N. Khaneja, S.J. Glaser, Phys. Rev. A **66**, 060301 (2002)
95. H. Yuan, S.J. Glaser, N. Khaneja, Phys. Rev. A **76**(1), 012316 (2007)
96. M. Nimbalkar, R. Zeier, J.L. Neves, S.B. Elavarasi, H. Yuan, N. Khaneja, K. Dorai, S.J. Glaser, Phys. Rev. A **85**, 012325 (2012)
97. M. Christandl, N. Datta, T.C. Dorlas, A. Ekert, A. Kay, A.J. Landahl, Phys. Rev. A **71**(3), 032312 (2005)
98. S.G. Schirmer, H. Fu, A.I. Solomon, Phys. Rev. A **63**, 063410 (2001)
99. C. Altafini, J. Math. Phys. **43**(5), 2051 (2002)
100. J.S. Hodges, J.C. Yang, C. Ramanathan, D.G. Cory, Phys. Rev. A **78**(1), 010303 (2008)
101. P. Cappellaro, L. Viola, C. Ramanathan, Phys. Rev. A **83**(3), 032304 (2011)
102. S.R. Clark, C.M. Alves, D. Jaksch, New J. Phys. **7**, 124 (2005)
103. D. Burgarth, K. Maruyama, F. Nori, Phys. Rev. A **79**, 020305 (2009)
104. C. DiFranco, M. Paternostro, M.S. Kim, Phys. Rev. Lett. **101**(23), 230502 (2008)
105. G.A. Álvarez, M. Mishkovsky, E.P. Danieli, P.R. Levstein, H.M. Pastawski, L. Frydman, Phys. Rev. A **81**(6), 060302 (2010)
106. D. Burgarth, V. Giovannetti, Phys. Rev. Lett. **99**(10), 100501 (2007)
107. J. Zhang, N. Rajendran, X. Peng, D. Suter, Phys. Rev. A **76**, 012317 (2007)

108. G.S. Boutis, D. Greenbaum, H. Cho, D.G. Cory, C. Ramanathan, Phys. Rev. Lett. **92**(13), 137201 (2004)
109. D. Greenbaum, M. Kindermann, C. Ramanathan, D.G. Cory, Phys. Rev. B **71**, 054403 (2005)
110. G.R. Khutsishvili, Sov. Phys. Uspekhi **8**(5), 743 (1966)
111. A.G. Redfield, Phys. Rev. **116**(2), 315 (1959)
112. D.K. Sodickson, J.S. Waugh, Phys. Rev. B **52**, 6467 (1995)
113. J.b. Waugh, Molecular Physics **95**(5), 731 (1998)
114. R. Bruschweiler, R. Ernst, Chem. Phys. Lett. **264**(3-4), 393 (1997)
115. A.K. Khitrin, B.M. Fung, J. Chem. Phys. **111**, 7480 (1999)
116. M.I. Kay, R.A. Young, A.S. Posner, Nature **204**(4963), 1050 (1964)
117. J.S. Prener, Journal of The Electrochemical Society **114**(1), 77 (1967)
118. W. Zhang, P. Cappellaro, N. Antler, B. Pepper, D.G. Cory, V.V. Dobrovitski, C. Ramanathan, L. Viola, Phys. Rev. A **80**(5), 052323 (2009)
119. C. Ramanathan, P. Cappellaro, L. Viola, D.G. Cory, New J. Phys. **13**(10), 103015 (2011)
120. E. Rufeil-Fiori, C.M. Sánchez, F.Y. Oliva, H.M. Pastawski, P.R. Levstein, Phys. Rev. A **79**(3), 032324 (2009)
121. W.V. der Lugt, W. Caspers, Physica **30**(8), 1658 (1964)
122. N. Leroy, E. Bres, Eur Cell Mater. **2**, 36 (2001)
123. R. Mazelsky, R. Hopkins, W. Kramer, Journal of Crystal Growth **3-4**, 260 (1968)
124. R. Mazelsky, R.C. Ohlmann, K. Steinbruegge, Journal of The Electrochemical Society **115**(1), 68 (1968)
125. S. Oishi, T. Kamiya, Nippon Kagaku Kaishi **9**, 800 (1994)
126. K. Teshima, S. Lee, K. Yubuta, Y. Kameno, T. Suzuki, T. Shishido, M. Endo, S. Oishi, Crystal Growth & Design **9**(9), 3832 (2009)
127. K. Teshima, S. Lee, T. Ishizaki, S. Mori, C. Mori, K. Yubuta, T. Ichiki, T. Shishido, S. Oishi, Cryst. Eng. Comm. **13**(6), 1749 (2011)
128. K. Teshima, S. Lee, M. Sakurai, Y. Kameno, K. Yubuta, T. Suzuki, T. Shishido, M. Endo, S. Oishi, Crystal Growth & Design **9**(6), 2937 (2009)
129. C.K. Hughes JM, Cameron M, Am Miner **74**, 870 (1989)
130. G. Cho, J.P. Yesinowski, Chem. Phys. Lett. **205**(1), 1 (1993)
131. Y. Pan, M.E. Fleet, Reviews in Mineralogy and Geochemistry **48**(1), 13 (2002)
132. Y. Pan, N. Chen, J.A. Weil, M.J. Nilges, American Mineralogist **87**(10), 1333 (2002)
133. N. Chen, Y. Pan, J.A. Weil, American Mineralogist **87**(1), 37 (2002)
134. G. Kaur, P. Cappellaro, New J. Phys. **14**(8), 083005 (2012)
135. M. Engelsberg, I.J. Lowe, J.L. Carolan, Phys. Rev. B **7**, 924 (1973)
136. A. Sur, I.J. Lowe, Phys. Rev. B **12**, 4597 (1975)
137. L.B. Moran, J.K. Berkowitz, J.P. Yesinowski, Phys. Rev. B **45**, 5347 (1992)
138. L.B. Moran, J.P. Yesinowski, Chemical Physics Letters **222**(4), 363 (1994)
139. G. Cho, J.P. Yesinowski, J. Chem. Phys. **100**(39), 15716 (1996)
140. H.J. Cho, P. Cappellaro, D.G. Cory, C. Ramanathan, Phys. Rev. B **74**(22), 224434 (2006)
141. G. Cho, C.N. Chau, J.P. Yesinowski, J. Phys. Chem. C **112**, 6165 (2008)
142. E.B. Fel'dman, S. Lacelle, J. Chem. Phys. **107**(18), 7067 (1997)
143. A.K. Khitrin, Chem. Phys. Lett. **274**, 217 (1997)
144. J.R. Goldman, T.D. Ladd, F. Yamaguchi, Y. Yamamoto, E. Abe, K.M. Itoh, in *Laser Spectroscopy* (World Scientific, 2002), pp. 333–336
145. M. Christandl, N. Datta, A. Ekert, A.J. Landahl, Phys. Rev. Lett. **92**, 187902 (2004)
146. M.E. Rose, *Elementary Theory of Angular Momentum* (New York: Wiley, 1957)
147. C. Ramanathan, H. Cho, P. Cappellaro, G.S. Boutis, D.G. Cory, Chem. Phys. Lett. **369**, 311 (2003)
148. S. Doronin, I. Maksimov, E. Fel'dman, JETP **91**, 597 (2000)
149. E. Lieb, T. Schultz, D. Mattis, Annals of Physics **16**, 407 (1961)
150. J. Fitzsimons, J. Twamley, Phys. Rev. Lett. **97**(9), 090502 (2006)
151. M. Markiewicz, M. Wiesniak, Phys. Rev. A **79**(5), 054304 (2009)
152. N.Y. Yao, L. Jiang, A.V. Gorshkov, Z.X. Gong, A. Zhai, L.M. Duan, M.D. Lukin, Phys. Rev. Lett. **106**(4), 040505 (2011)

153. A. Kay, Phys. Rev. Lett. **98**(1), 010501 (2007)
154. A. Kay, Int. J. of Quantum Info. **8**(4), 641 (2010)
155. G.M.P. C. Di Franco, M. Paternostro, Int. J. Quant. Inf. **6**, 659 (2008)
156. S.R. Clark, A. Klein, M. Bruderer, D. Jaksch, New J. Phys. **9**(6), 202 (2007)
157. D. Burgarth, K. Maruyama, F. Nori, New J. Phys. **13**(1), 013019 (2011)
158. C. Di Franco, M. Paternostro, M.S. Kim, Phys. Rev. Lett. **102**, 187203 (2009)
159. M.K. Henry, C. Ramanathan, J.S. Hodges, C.A. Ryan, M.J. Ditty, R. Laflamme, D.G. Cory, Phys. Rev. Lett. **99**(22), 220501 (2007)
160. A. Davis, G. Estcourt, J. Keeler, E. Laue, J. Titman, J. Mag. Res. **105**(2), 167 (1993)
161. P. Cappellaro, Quantum information processing in multi-spin systems. PhD dissertation, Massachusetts Institute of Technology, Department of Nuclear Science and Engineering (2006)
162. E.B. Fel'dman, S. Lacelle, Chem. Phys. Lett. **253**(1-2), 27 (1996)
163. S. Doronin, E. Fel'dman, I. Maximov, Journal of Magnetic Resonance **171**(1), 37 (2004)
164. D.F.V. James, P.G. Kwiat, W.J. Munro, A.G. White, Phys. Rev. A **64**(5), 052312 (2001)
165. T.J. Osborne, N. Linden, Phys. Rev. A **69**(5), 052315 (2004)
166. Y. Li, T. Shi, B. Chen, Z. Song, C.P. Sun, Phys. Rev. A **71**, 022301 (2005)
167. A. Wojcik, T. Luczak, P. Kurzynski, A. Grudka, T. Gdala, M. Bednarska, Phys. Rev. A **72**, 034303 (2005)
168. G. Gualdi, V. Kostak, I. Marzoli, P. Tombesi, Phys. Rev. A **78**(2), 022325 (2008)
169. A. Ajoy, P. Cappellaro, ArXiv:1207.5580 (2012)
170. B. Furman, in *HFI/NQI 2007*, ed. by A. Pasquevich, M. Rentera, E. Saitovitch, H. Petrilli (Springer Berlin Heidelberg, 2008), pp. 459–465
171. H.G. Krojanski, D. Suter, Phys. Rev. Lett. **93**(9), 090501 (2004)
172. T.W. Borneman, Control methods for spin-actuator multinode quantum information processing. Ph.D. thesis, Massachusetts Institute of Technology (2012)
173. J. Le Moigne, J.L. Gallani, P. Wautelet, M. Moroni, L. Oswald, C. Cruz, Y. Galerne, J.C. Arnault, R. Duran, M. Garrett, Langmuir **14**(26), 7484 (1998)
174. M. Mannini, L. Sorace, L. Gorini, F.M. Piras, A. Caneschi, A. Magnani, S. Menichetti, D. Gatteschi, Langmuir **23**(5), 2389 (2007)
175. M.V.G. Dutt, L. Childress, L. Jiang, E. Togan, J. Maze, F. Jelezko, A.S. Zibrov, P.R. Hemmer, M.D. Lukin, Science **316**, 1312 (2007)
176. P. Cappellaro, L. Jiang, J.S. Hodges, M.D. Lukin, Phys. Rev. Lett. **102**(21), 210502 (2009)
177. N. Yao, L. Jiang, A. Gorshkov, P. Maurer, G. Giedke, J. Cirac, M. Lukin, Nat Commun **3**, 800 (2012)
178. Y. Ping, B.W. Lovett, S.C. Benjamin, E.M. Gauger, Phys. Rev. Lett. **110**, 100503 (2013)
179. C.D. Weis, A. Schuh, A. Batra, A. Persaud, I.W. Rangelow, J. Bokor, C.C. Lo, S. Cabrini, E. Sideras-Haddad, G.D. Fuchs, R. Hanson, D.D. Awschalom, T. Schenkel, J. Vac. Sc. & Tech. B **26**(6), 2596 (2008)
180. D.M. Toyli, C.D. Weis, G.D. Fuchs, T. Schenkel, D.D. Awschalom, Nano Letters **10**(8), 3168 (2010)
181. B. Naydenov, V. Richter, J. Beck, M. Steiner, P. Neumann, G. Balasubramanian, J. Achard, F. Jelezko, J. Wrachtrup, R. Kalish, App. Phys. Lett. **96**(16), 163108 (2010)
182. P. Spinicelli, A. Drau, L. Rondin, F. Silva, J. Achard, S. Xavier, S. Bansropun, T. Debuisschert, S. Pezzagna, J. Meijer, V. Jacques, J.F. Roch, New J. Phys. **13**(2), 025014 (2011)
183. R. Hanson, F.M. Mendoza, R.J. Epstein, D.D. Awschalom, Phys. Rev. Lett. **97**(8), 087601 (2006)
184. P.C. Maurer, J.R. Maze, P.L. Stanwix, L. Jiang, A.V. Gorshkov, A.A. Zibrov, B. Harke, J.S. Hodges, A.S. Zibrov, A. Yacoby, D. Twitchen, S.W. Hell, R.L. Walsworth, M.D. Lukin, Nat. Phys. **6**, 912 (2010)
185. E. Rittweger, D. Wildanger, S.W. Hell, Europhys. Lett. **86**(1), 14001 (2009)
186. A. Wójcik, T. Łuczak, P. Kurzyński, A. Grudka, T. Gdala, M. Bednarska, Phys. Rev. A **75**, 022330 (2007)
187. L. Banchi, T.J.G. Apollaro, A. Cuccoli, R. Vaia, P. Verrucchi, New Journal of Physics **13**(12), 123006 (2011)

188. P.C. Maurer, G. Kucsko, C. Latta, L. Jiang, N.Y. Yao, S.D. Bennett, F. Pastawski, D. Hunger, N. Chisholm, M. Markham, D.J. Twitchen, J.I. Cirac, M.D. Lukin, Science **336**(6086), 1283 (2012)
189. N. Bar-Gill, L.M. Pham, A. Jarmola, D. Budker, R.L. Walsworth, ArXiv:1211.7094 (2012)
190. J.M. Taylor, P. Cappellaro, L. Childress, L. Jiang, D. Budker, P.R. Hemmer, A. Yacoby, R. Walsworth, M.D. Lukin, Nature Phys. **4**(10), 810 (2008)
191. P. Maletinsky, S. Hong, M.S. Grinolds, B. Hausmann, M.D. Lukin, R.L. Walsworth, M. Loncar, A. Yacoby, Nat Nano **7**(5), 320 (2012)
192. P. Rabl, S.J. Kolkowitz, F.H.L. Koppens, J.G.E. Harris, P. Zoller, M.D. Lukin, Nat Phys **6**(8), 602 (2010)
193. J. Cai, A. Retzker, F. Jelezko, M.B. Plenio, Nat Phys. **9**(3), 168 (2013)

# Index